Dual-Aircraft Investigation of the Inner Core of Hurricane Norbert. Part I: Kinematic Structure

FRANK D. MARKS, JR.

Hurricane Research Division, NOAA/AOML, Miami, Florida

ROBERT A. HOUZE, JR.

Department of Atmospheric Sciences, University of Washington, Seattle, Washington

JOHN F. GAMACHE

Hurricane Research Division, NOAA/AOML, Miami, Florida

(Manuscript received 27 November 1990, in final form 9 September 1991)

ABSTRACT

On 24–25 September 1984 air motions and physical processes in the eyewall region of Hurricane Norbert were investigated with two National Oceanic and Atmospheric Administration (NOAA) Aircraft Operations Center (AOC) WP-3D research aircraft. One aircraft, equipped with the airborne Doppler radar, flew repeated radial penetrations of the eyewall, mapping the three-dimensional wind field throughout a 40-km radius of the storm center. These data provide the first complete documentation of the three-dimensional wind field of the inner core of a hurricane on spatial scales of 10–25 km in the horizontal and 1 km in the vertical and temporal scales of 1–2 h.

The wind field was asymmetric, and the asymmetry varied with altitude. As altitude increased the location of the maximum tangential wind sloped upwind, from left of the storm track at 1-km altitude to right of the storm track above 3 km. The radial wind at 1-km altitude was inward in front of the storm and outward behind. This pattern in the radial flow reversed above 3-km altitude, with inflow at the rear of the storm and outflow in the front. The maximum vertical velocity was located to the left of the storm track at all levels. This maximum sloped downwind, increasing in altitude from 2 km in front of and to the left of the track to 8 km behind and to the right of the track.

To investigate the nature of the wind field asymmetry, the horizontal wind components were partitioned into a horizontal mean wind, varying with altitude and a perturbation wind. The cylindrical nature of the wind field permitted further partitioning of the perturbation wind into the mean vortex and a perturbation from the mean vortex. The mean wind derived from the partitioning agreed with synoptic analyses and was consistent with past studies—lying about 20° to the right of the storm motion. The symmetric vortex structure was consistent with past studies when it is taken into consideration that Norbert was a weakening storm. The asymmetric perturbation field had a distinct signature at both lower and upper levels. At 1 km, the asymmetric perturbation had the form of a source-sink field. The source and sink points were at the radius of maximum wind with the convergent sink on the leading, inflow side of the vortex and the divergent source on the trailing, outflow side of the vortex. At 3 km and higher, the asymmetric wind fields had the character of a vortex couplet with cyclonic and anticyclonic gyres in the right-front and left-rear quadrants of the storm, respectively, and stagnation points at the radius of maximum wind on the upwind, trailing and downwind, leading side of the storm.

1. Introduction

Since 1982, the Hurricane Research Division has used the NOAA prototype airborne Doppler radar to record the three-dimensional wind and reflectivity data in the inner core of tropical cyclones (Marks and Houze 1984, 1987). These observations have shown the utility of the airborne Doppler radar to sample the wind field in three dimensions with high spatial (~1 km) and temporal (~0.5–1.0 h) resolution. Before the advent of the airborne Doppler, details of the kinematic structure of the inner core of tropical cyclones were determined by combining aircraft observations from one or more aircraft at different flight levels over a 4–6-h period (e.g., LaSeur and Hawkins 1963; Hawkins and Rubsam 1968; Hawkins and Imbembo 1976; Jorgensen 1984b; Frank 1984), from a composite of rawinsonde observations from many different stations over a 12–24-h period (e.g., Frank 1977), or from a composite of flight-level data obtained in many storms (Shea and Gray 1973; Gray and Shea 1973; Willoughby et al. 1982; Jorgensen 1984a). While these studies provided

Corresponding author address: Dr. Frank Marks, Jr., NOAA/AOML, Hurricane Research Division, 4301 Rickenbacker Causeway, Miami, FL 33149.

extensive information on the axisymmetric structure of the vortex and some aspects of asymmetries, the large sampling time needed to construct the composite fields limited the ability to determine details of the asymmetric structure of the wind field.

Airborne Doppler data, collected from two nearly orthogonal flight legs, can be combined in a "pseudo" dual-Doppler analysis ("pseudo" because it uses data from the same radar at two times) of the three-dimensional wind field. The derived Doppler wind fields cover horizontal and vertical dimensions of ~75–100 km and 15 km, respectively. The three-dimensional wind analyses cover 0.5–1.0-h intervals (equivalent to a one-dimensional sample of flight-level winds 200–400 km in length), compared with the 4–6 h needed for the composite analyses of flight-level data (e.g., LaSeur and Hawkins 1963; Hawkins and Rubsam 1968; Hawkins and Imbembo 1976; Jorgensen 1984b). Hence, storm structure on scales of 50 km and 1–2 h, especially asymmetries, that were difficult to infer from the composite analyses can now be deduced.

Airborne Doppler observations were used first to describe the developing Tropical Cyclone Debby (Marks and Houze 1984), then later to study the mature phase of Hurricane Alicia as it crossed the Gulf of Mexico toward landfall near Galveston, Texas (Marks and Houze 1987). Dual-Doppler analyses revealed that, to a first approximation, the eyewall of Alicia was two-dimensional and dominated by the primary (azimuthal) and secondary (radius–height) circulations of the vortex. The primary circulation consisted of a core of maximum tangential wind that sloped radially outward with increasing height. The slope of the maximum tangential wind was similar to the slope deduced in the composites of flight-level data (Willoughby et al. 1982; Jorgensen 1984a,b) and in model simulations (Willoughby et al. 1984b). The peak winds were observed at low levels (1.5–2.5 km).

The secondary circulation was characterized by a lower tropospheric layer of inward-directed flow that extended well above the boundary layer in the vicinity of the eyewall. The maximum inflow was at 2.0–4.5

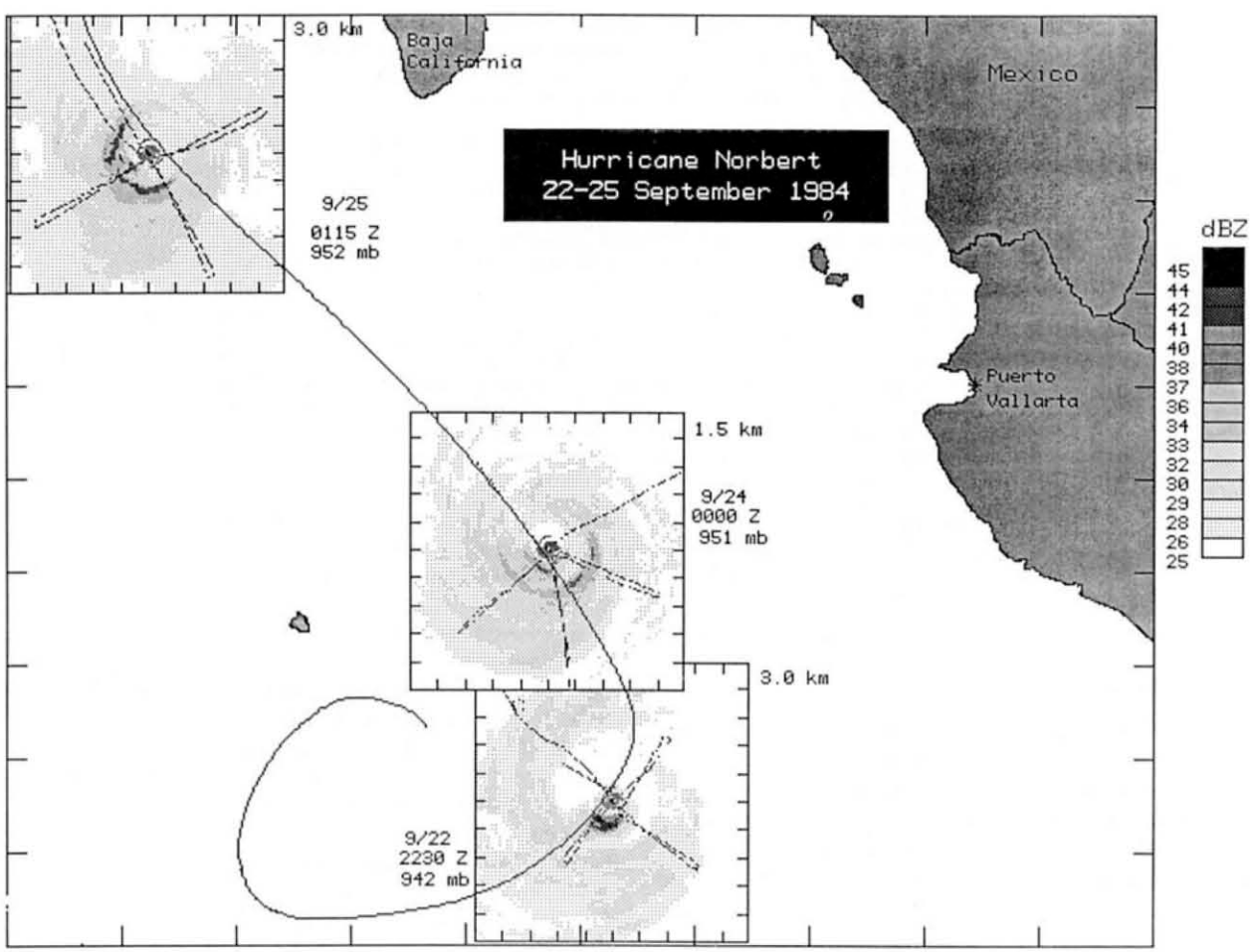

FIG. 1. Track of Hurricane Norbert for 22–25 September 1984. The radar time composites indicate the periods of the research flights into the storm. Each radar composite represents a domain 200 km on a side, with tick marks at 20-km intervals. The tick marks on the outer domain are 85 km in the horizontal and 68 km in the vertical. The aircraft flight tracks are indicated by the dashed lines in each composite. Reflectivities are depicted as increasing shades of gray for thresholds of 26, 29, 33, 37, and 41 dBZ.

km. A layer of intense radial outflow from the eyewall was concentrated at upper levels (10–14 km). The airborne Doppler data provided observational confirmation of the upper-tropospheric portion of the secondary circulation predicted by numerical model simulations (e.g., Willoughby et al. 1984b), which occurs at altitudes higher than can be reached by hurricane research aircraft.

The Alicia analyses also revealed some asymmetries in the secondary circulation that were consistent with the theoretical and observational studies of Shapiro (1983) and Willoughby et al. (1984a). The Doppler observations in Alicia showed an asymmetry in the eyewall mesoscale updraft at the top of the boundary layer, as discussed by Shapiro, which extended throughout the depth of the eyewall. The front–back asymmetry in the eyewall updraft resulted in a front–back asymmetry in the height of the outflow layer. The height of the outflow was 1.5–2.0 km lower behind the storm than it was in the front. East–west asymmetries in the inflow at low levels (1.5–5.0-km altitude), similar to that described by Willoughby et al. (1984a) and Powell (1982), were observed.

The objective of this paper is to extend the results of Marks and Houze (1984, 1987) by providing a more complete three-dimensional mapping of the inner core of a hurricane by Doppler radar. In particular, more details of the asymmetric structure are sought. The Doppler analysis for Hurricane Norbert is expanded over that used in the previous studies to include the derivation of the vertical wind component. In addition, the accuracy of the wind field analysis is discussed. A technique is outlined to separate the derived wind field into a large-scale mean wind that varies with height, a symmetric mean vortex, and wavenumber one and higher asymmetries. Trajectories of mesoscale air motions within the inner core of the storm are constructed from the three-dimensional wind field. This paper also extends the previous work by considering a storm that, though still strong, was in a dissipating stage, whereas Debby was developing and Alicia was mature.

2. Storm history

Hurricane Norbert formed in the eastern Pacific Ocean on 16 September 1984. The storm track in Fig. 1 shows that over the next 6 days, the storm track made a cyclonic loop. On 23 September the storm took a more linear track toward the northwest, passing ~220 km to the west of Baja California. Three successive research flights were flown in the storm from 22 to 25 September. During the period of the first two research flights, the storm weakened. The central pressure decreased from 942 hPa on 22 September to 951 hPa on 24 September. Coincident with the pressure rise, the storm underwent a concentric eyewall cycle (Willoughby et al. 1984a). Figure 1 shows that on 22 September the horizontal precipitation structure was characterized by concentric eyewalls: the inner eyewall with a diameter of 25 km and the outer eyewall with a diameter of 90 km. By 24 September the outer eyewall contracted to ~60 km in diameter, while the remains

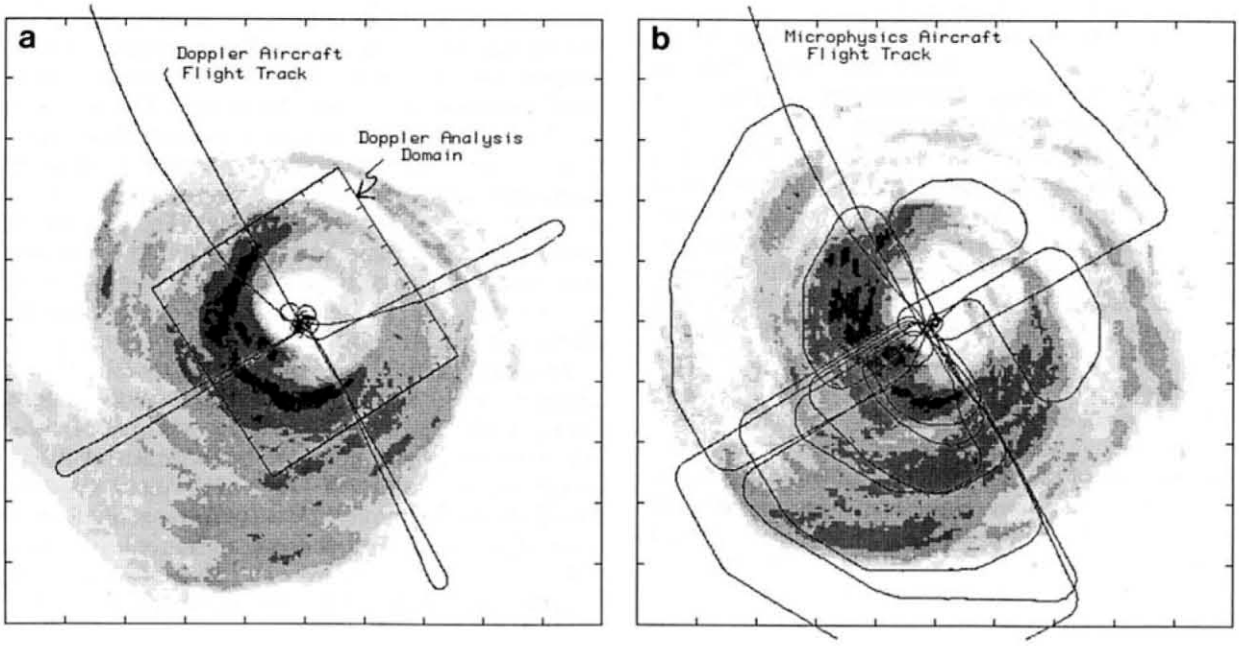

FIG. 2. Flight tracks in Hurricane Norbert. Gray shades show reflectivity of increasing intensity for thresholds of 28, 29, 31, 34, 38, and 42 dBZ. The region covered by the radar composite is 200 × 200 km. The inner box in (a) is 75 km on a side rotated along the storm track (327°). The tick marks on the outer domain are 20 km apart. Tick marks on the inner box in (a) are 7.5 km apart. The aircraft flight tracks are denoted by the thin solid lines. The storm wind center deduced from the flight-level data is indicated by the hurricane symbol.

of the inner eyewall were visible inside the southwest quadrant of the outer eyewall at a radius of 13 km.

The airborne Doppler data analyzed in this study were collected during the third day (25 September 1984) when the storm was 250 km west-southwest of the southern tip of Baja California and moving northwestward (toward 327°) at 5.6 m s^{-1}. The minimum central pressure (extrapolated from 3-km altitude) was 952 hPa at 0030 UTC 25 September, when the experiment began. Over the first 2.5 h of the experiment (0030–0310 UTC), the storm filled slowly (~1 hPa h^{-1}), while over the next 2 h (0310–0508 UTC) the storm filled at an average rate of almost 2 hPa h^{-1}. Over the 4.5-h period, the maximum flight-level winds at 3-km altitude decreased from 55 to 49 m s^{-1}. Figures 1 and 2a show that the outer eyewall had continued to contract, from a diameter of 60 km on 24 September to 52 km during the flight. A portion of the inner eyewall was still present at a radius of 15 km along the west-southwest portion of the outer eyewall.

At landfall (0700 UTC 26 September), 27 h after the end of the last research flight, the storm had weakened considerably, and peak winds were only 28 m s^{-1}. The rapid weakening was correlated with the storm passing over a region of cold sea surface temperatures (<25°C) during the 24 h before landfall. Gunther and Cross (1985) present a detailed description of the synoptic-scale evolution of Hurricane Norbert.

3. Data

a. Flight tracks

The three-dimensional wind analysis covers the period 0018–0215 UTC 25 September 1984, when the storm was filling slowly. The flight tracks of both the lower-level (3 km) Doppler radar aircraft and the upper-level (6 km) cloud physics aircraft are shown in Fig. 2. The flight tracks are superposed on time composites of the radar reflectivity pattern. The Doppler aircraft flew repeated radial penetrations in and out of the eyewall with 90° turns in the eye at 3-km altitude (Fig. 2a). The resultant "L-shaped" patterns were flown to facilitate good dual-Doppler coverage in each quadrant of the eyewall region out to a radius of 40 km from the storm center. The flight track of the upper-level aircraft consisted of a sequence of overlapping wedge-shaped circuits that covered all portions of the storm. The majority of these tracks were flown in the active southwestern quadrant. The data collected from the upper-level aircraft are the subject of Part II of this study.

b. Radar reflectivity data

Each NOAA WP-3D aircraft is equipped with two quantitative radars. A horizontally scanning C-band (5.5-cm wavelength) radar antenna is in the lower fuselage. A vertically scanning X-band (3.2-cm wavelength) radar antenna is in the tail section. Characteristics of these radars are given by Jorgensen (1984a).

Except for the echo patterns in Figs. 1–2, which are derived from the lower fuselage (LF) radar, this paper uses data from the tail (TA) radars. The TA radars provide three-dimensional mapping of the reflectivity, since they scan vertically in a plane perpendicular to the ground track of the aircraft. The horizontal reflectivity patterns derived from the TA radars in this storm are consistent with those from the LF radars, despite the LF radar's advantage of reduced effects of intervening attenuation. Three-dimensional time-composite reflectivity patterns were constructed from the TA radar data collected by the WP-3D aircraft according to the procedures described by Marks and Houze (1984).

c. Doppler radar data

The airborne Doppler radar data were collected with the TA radar of the lower aircraft. The antenna pointed at right angles to the aircraft's ground track while sweeping through elevation angles of 0°–360°. Thus, the Doppler radar measured the component of the precipitation particle motion perpendicular to the flight track. Both wind and vertical motions of the precipitation particles affected the measured velocity along the radar beam. The antenna rotated at one revolution per 7.5 s. This rate provided data at all elevation angles once every 0.8 km of flight track.

The three-dimensional wind field within 39 km of the storm center was derived from a "pseudo" dual-Doppler analysis in each quadrant of the storm. Each flight leg used in the dual-Doppler analysis was ~75 km long and lasted 10–11 min. The airborne Doppler data extended 39 km in range from the radar, with a radial resolution of 150 m. Hence, only the inner 39 km of each flight leg was used for the dual-Doppler analysis. The 39-km maximum dimension resulted in a maximum time separation of 12 min between Doppler radial velocities from the two legs. The minimum separation was 2.5 min at the turn points. Outside turns, where the plane turns opposite to the intended direction of flight, were used to improve overlap of radial velocities from the two legs near the turn point.

The average time separation between radial velocity estimates was 7.25 min, implying that there was a possibility of deriving estimates of convective-scale motions. However, the strength of the tangential wind in the eyewall region (~40–50 m s^{-1}) ruled this out. During the average time separation, a tangential wind speed of 50 m s^{-1} advected an air parcel ~22 km (~48° of azimuth at the eyewall radius of 26 km). In the same interval, a radial wind speed of 5 m s^{-1} advected the air parcel only 2 km. Because of these limitations and differences in azimuthal and radial resolution, this analysis concentrates on the mesoscale motions within the eyewall circulation with time scales of

10–15 min and space scales of 20°–25° in azimuth and 2–4 km in radius.

d. Doppler analysis procedure

The horizontal wind field in three dimensions was determined for each quadrant using the technique of Jorgensen et al. (1983), as modified by Marks and Houze (1984, 1987) for a moving vortex. The storm motion was determined from the flight-level data using the technique of Willoughby and Chelmow (1982).

Divergence was computed from the horizontal wind estimates at each point in the analysis domain. The vertical wind components were derived by integrating the anelastic continuity equation downward using a boundary condition of zero vertical motion at the top of the radar echoes (10–12-km altitude). Corrections for the vertical velocity were then made to the horizontal winds. New estimates of divergence and vertical velocity were obtained from these winds. This procedure was repeated until the mean of the absolute value of the change in horizontal wind components at each level from one iteration to the next was <0.1 m s^{-1} (usually within two iterations).

The Doppler-derived wind fields for the four quadrants were combined to form a storm-composite wind field that was 75 × 75 km on a side and centered on the storm circulation center. The wind field extended from 0.5 to 12.0 km in altitude. Any gaps in the composite wind field caused by missing Doppler wind estimates (i.e., a missing wind component from one of the legs in an L-shaped pattern) were filled using an iterative-filling and -filtering scheme. Taking advantage of the circular symmetry of the vortex wind structure, we used a Gaussian filter in azimuth and radius to fill the holes and seams between each "L" in the composite wind analysis. The *e*-folding distances of the Gaussian filter were 20° in azimuth and 2 km in radius. At the radius of maximum wind (~26 km) the resultant azimuthal *e*-folding distance was 7 km.

The composite analysis was then matched to the filled values with a multipass filtering scheme. The filter, designed by Leise (1981), was applied to the filled winds several times, with the short-wave cutoff decreasing each time the filter was applied (e.g., $8\Delta x$ on the first pass, $4\Delta x$ on the second pass, and $2\Delta x$ on the last pass). After each filter application, the original composite wind values were reinserted into the filtered wind analysis. Hence, the filter was only being applied to the holes and not the original winds. The final step in the process was to filter the original winds and the filtered winds in the holes with a $2\Delta x$ cutoff. Divergence and vertical velocity were recomputed for each point in the domain.

The reflectivity value at each point in the wind analysis was checked, and the wind values with corresponding reflectivity values < 1 dBZ were deleted to prevent the filter/filling process from generating circulations where no data existed.

e. Doppler data quality

The quality of the Doppler-derived winds was examined through comparison with the aircraft winds measured along the flight tracks at 3- and 6-km altitude. A detailed comparison was made between the Doppler estimates of the u, v, and w components of the wind and the nearest flight-level wind value in the vertical and the horizontal. Only flight-level winds within 250 m in the vertical and 1 km in the horizontal of a Doppler estimate were included in the intercomparison (points included were typically within 100 m in the vertical and 300 m in the horizontal). The original flight-level wind values were at 1-s intervals, representing a horizontal spacing of ~150 m, much smaller than that represented by the Doppler estimates. Because of the small horizontal spacing between data points, the flight-level data were filtered to a scale as comparable to that of the Doppler estimates. The Doppler estimates, with a horizontal resolution of 1.5 km, resolved features in the wind field with horizontal scales of 4–5 km. The flight-level wind components were low-pass filtered by a least-squares fit to the data, using a cubic spline combined with a derivative constraint (Ooyama 1987). The derivative constraint used in this analysis had a filter response that removed temporal scales < 15 s (horizontal scale ~ 2.25 km) and fully resolved scales > 30 s (>4.5 km).

Figure 3 shows a comparison of the filtered flight-level wind components nearest in space to the Doppler data values and the Doppler-derived wind components for the aircraft with the Doppler radar at 3 km. Figure 4 shows a similar comparison for the aircraft at 6 km. Figures 3a and 3b show good agreement between the horizontal wind components, with a nearly one-to-one correspondence between the values. Linear fits to the data points in Figs. 3a and 3b had slopes of 0.94 and 0.98 for u and v, respectively. The correlation coefficient for both fits was 0.98. There was some variability in the Doppler-derived estimates, with a standard deviation in both horizontal components of 2.7 m s^{-1}. The Doppler winds overestimated the westerly wind component by 3.6 m s^{-1}, while the v component had only a slight bias (0.5 m s^{-1}). The magnitude of the deviations was comparable with those found by Marks and Houze (1984, 1987) and Jorgensen et al. (1983). The mean difference between the flight-level and Doppler-derived winds at 3 km was 260° at 3.5 m s^{-1}.

As at 3 km, the comparison of the horizontal wind components at 6 km showed good agreement between the Doppler-derived and flight-level winds (Figs. 4a and 4b). Linear fits to the data values in Figs. 4a and 4b had slopes of 0.90 and 0.96 for u and v, respectively. The correlation coefficient for both fits, 0.94, was not as high as at 3 km. The standard deviation for the u component was higher than those for any of the other wind components, 3.3 m s^{-1} versus 2.4 m s^{-1} for the v component. Both the u and v components of the Doppler estimates had slight positive biases of 2.5–3.5

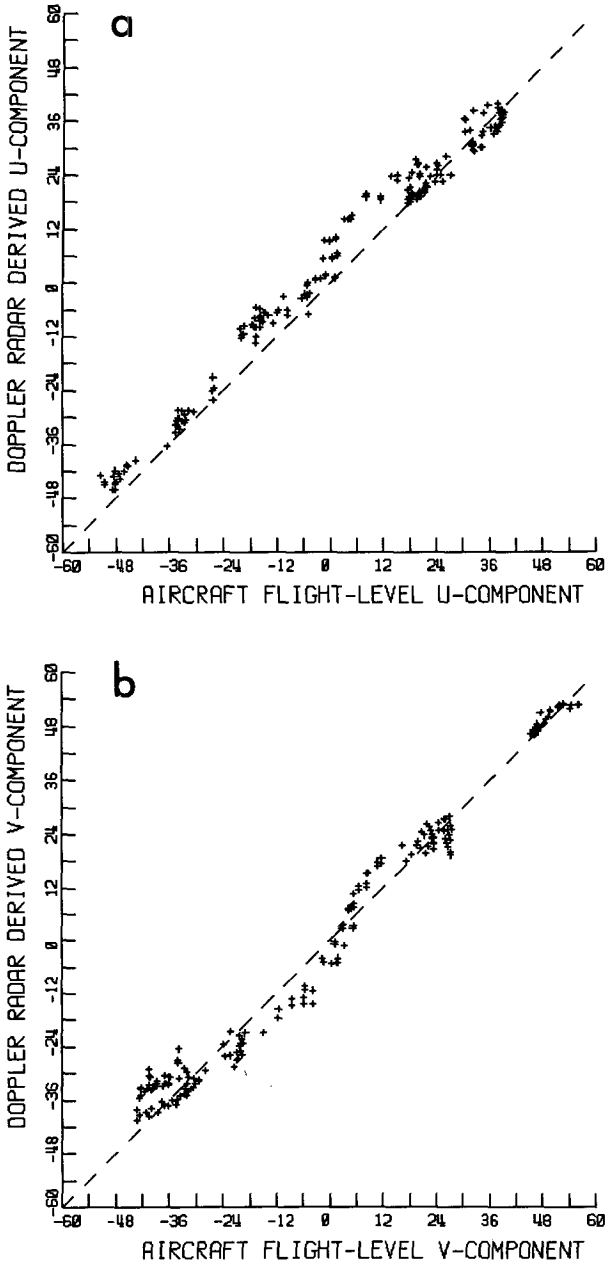

FIG. 3. Scatterplots of mean aircraft flight-level (a) u- and (b) v-wind components for the aircraft at 3-km altitude versus the Doppler-derived wind components at the same position. The diagonal dashed lines denote a one-to-one correspondence.

m s^{-1}. In particular, several points of the u component of the Doppler estimates had 5–6 m s^{-1} too much (too little) westerly (easterly) component. The wind observations at 6 km were not well distributed around the storm, as 90% of the values were obtained in the quadrant south of the storm center (Fig. 2b). The uneven distribution of flight-level winds coupled with possible navigation errors between the two aircraft was probably the cause of the relatively large bias in the u component. The mean difference between the flight-level and the Doppler-derived winds was from 225° at 4.5 m s^{-1}.

A point-by-point comparison of vertical wind (w) estimates at both levels showed a weak linear relationship between the Doppler-derived and flight-level values. This result is not surprising, considering that the Doppler-derived vertical winds came from an integration of divergence values computed with data values 3 km apart and representing a 9 km^2 area. This effective spatial averaging altered the magnitude of the w components as well as the relative locations of the up and down motions. Hence, it is reasonable only to compare

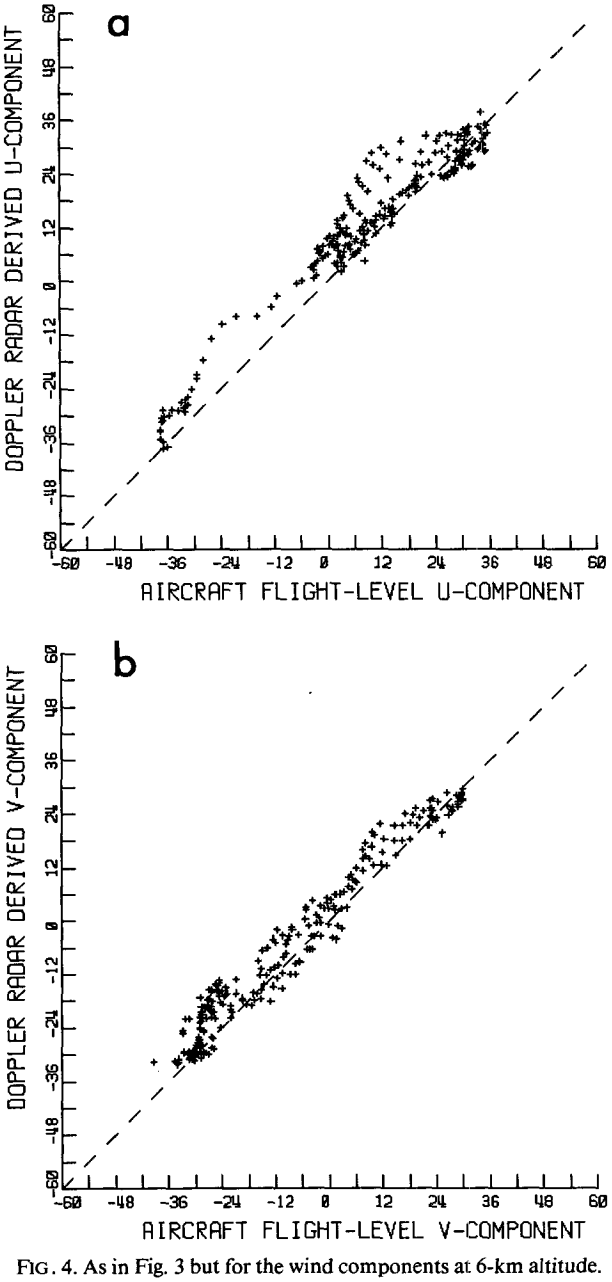

FIG. 4. As in Fig. 3 but for the wind components at 6-km altitude.

the statistics of the two distributions. Table 1 lists the characteristics of these distributions; Fig. 5 depicts the frequency distribution of the w components.

There are no significant differences in the distributions between the flight-level and the Doppler-derived vertical winds. In the mean, the flight-level vertical winds were 40–50 cm s^{-1} larger than the Doppler-derived values. Figure 5a shows that at 3 km, the flight-level values had fewer downdrafts than the Doppler estimates—25% versus 31%. Marks and Houze (1987) noted a similar characteristic when comparing the distribution of vertical-incidence Doppler estimates of w to those derived by Jorgensen et al. (1985) for flight-level data, suggesting that the flight-level data underestimated the magnitude of the downdrafts. At 6 km, however, the percentage of downdrafts observed in the flight-level data was equivalent to that determined from the Doppler analysis (Fig. 5b).

Both distributions had similar standard deviations. That of the Doppler-derived w component was 5–10 cm s^{-1} larger on the average. However, Fig. 5 shows that at both altitudes, the Doppler w components were more evenly distributed around 0 m s^{-1} than the flight-level values. The mean vertical winds from both distributions had increasing values with increasing altitude.

4. Relative wind field

a. Horizontal analyses

The Doppler analysis renders a wind field relative to the ground, the "total" wind field, in a storm-centered coordinate system. Historically, observational studies of the kinematic structure of hurricanes have discussed the "relative" wind, that is, the circulation relative to the moving storm. In a cylindrical coordinate system centered on the storm, the horizontal relative wind vector $\mathbf{v}_r$ can be expressed as

$$\mathbf{v}_r(r, \lambda, z) = \mathbf{v}(r, \lambda, z) - \mathbf{v}_s, \qquad (1)$$

where $\mathbf{v}$ is the total wind, $\mathbf{v}_s$ is the horizontal storm-motion vector (a constant defined by the objective fit to the flight-level data), r is radius, λ is azimuth, and z is height. The Doppler-derived field of $\mathbf{v}_r$ is shown in Fig. 6. The circulation within the eyewall region of the storm is depicted by this field.

TABLE 1. Characteristics of the vertical wind distributions for the flight-level and Doppler-derived winds.

	3 km		6 km	
	Doppler	Flight level	Doppler	Flight level
Mean (m s^{-1})	−0.13	0.36	0.18	0.68
Standard deviation (m s^{-1})	1.60	1.80	1.90	1.60
Points	190		259	

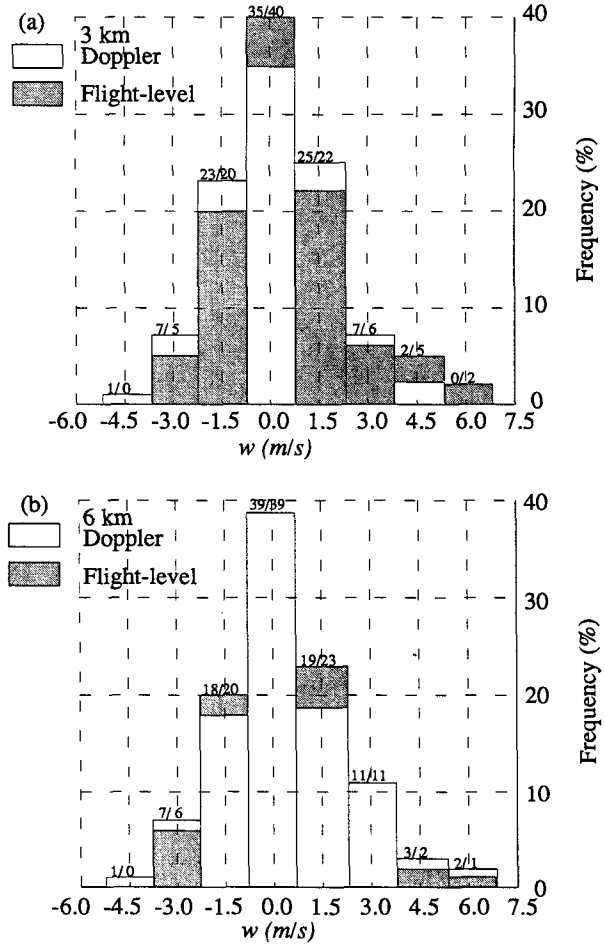

FIG. 5. Frequency distribution of the w component of the wind from flight-level (solid) and from the Doppler analysis (open) at (a) 3-km and (b) 6-km altitude. The frequency is plotted as a percentage of the total points at each altitude (given in Table 1). The points are grouped into classes 1.5 m s^{-1} wide. Percent in each class is listed (Doppler/flight level).

The strong tangential motion seen surrounding the center is characteristic of tropical cyclones. It increased with radius from the center to ~26 km (the radius of maximum wind) and then decreased outside this radius. As in the Alicia wind field analyzed by Marks and Houze (1987), the radius of maximum wind increased with increasing altitude, from 23 km at 1-km altitude to 34 km at 12 km, while the intensity of the circulation decreased with altitude above 3 km.

The asymmetry of the wind and the reflectivity fields is also evident in Fig. 6. The reflectivity was maximum to the left of the SE-to-NW storm track at all levels. However, whereas the reflectivity asymmetry was the same at all altitudes, the wind field asymmetry varied with height. At 1 km (Fig. 6a) the peak wind speed of 60 m s^{-1} was in the west-southwest portion of the eyewall at a radius of 23 km, matching the position of the peak reflectivity values. At 3 (Fig. 6b), 6 (Fig. 6c), 9

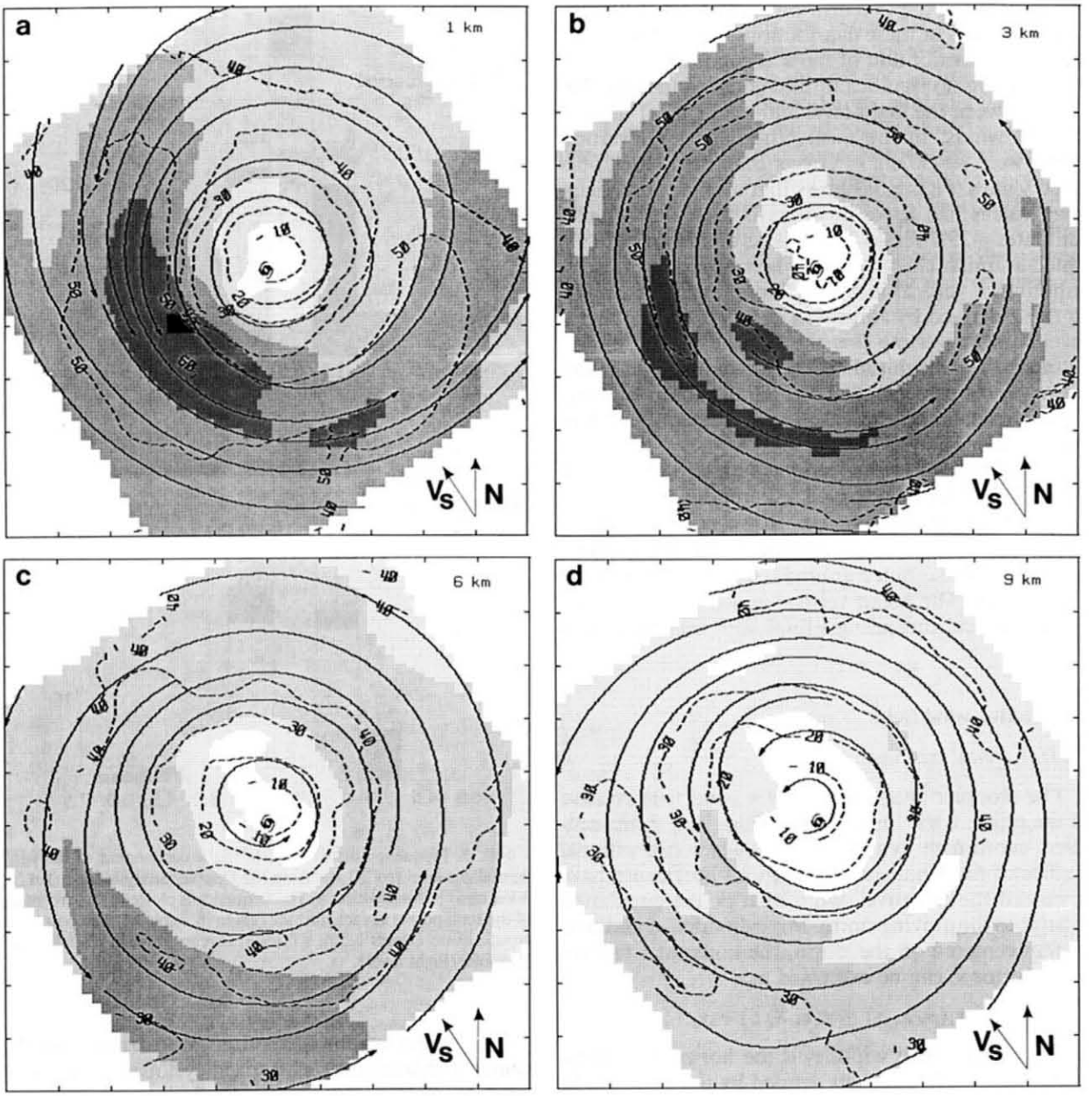

FIG. 6. Total horizontal wind field (streamlines and isotachs) superposed on the reflectivity (dBZ). The domain of the analysis is 82.5 km on a side centered on the storm (hurricane symbol). Tick marks are at 8.25-km intervals. Reflectivity values are depicted by increasing shades of gray at 10, 20, 30, 40, and 44 dBZ. The streamlines are denoted by solid lines and the isotachs by dashed lines. There are no data values for the triangular regions in each corner because they are outside of the Doppler analysis domain.

(Fig. 6d), and 12 km (Fig. 6e) the peak wind speeds were in the northeast portion of the eyewall, nearly 180° out of phase with the peak reflectivity values.

The vertical velocity field shown in Fig. 7 was also asymmetric across the track, having $w > 0$ primarily to the left of track and $w < 0$ to the right of track—similar to the reflectivity asymmetry. The w maxima were at the same radius and slightly upwind of the reflectivity maxima at each altitude. The peak updraft magnitudes, estimated from the Doppler analysis ($\sim$6 m s^{-1}), were comparable with the upper 10% of the cores in the population described by Jorgensen et al. (1985). These peak updrafts were found near the radius of maximum winds in the southwest quadrant at 3- and 6-km altitude (Figs. 7b and 7c).

While the magnitude of the peak drafts was comparable with those of the cores described by Jorgensen et al. (1985), the area covered by drafts of this magnitude was much lower. At all levels, the region of upward motion > 3 m s^{-1} was confined into a narrow

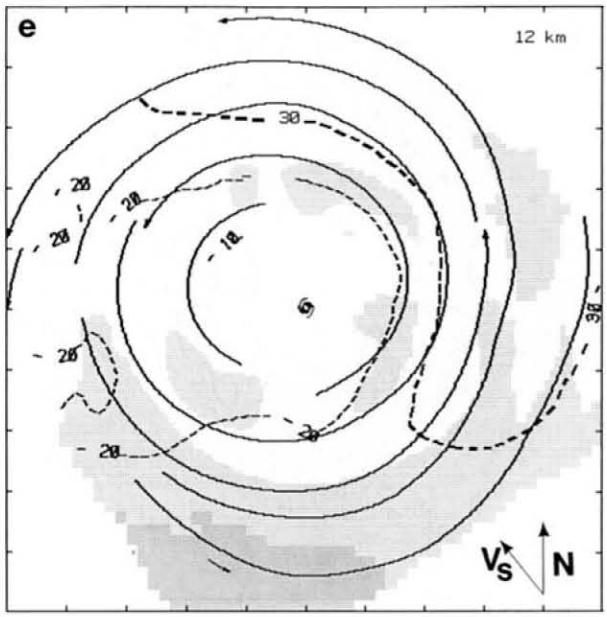

FIG. 6. (*Continued*)

strip that was 6–8 km wide and 20–25 km long in the west and southwest portion of the eyewall. Updrafts > 3 m s^{-1} made up <5% of the eyewall region [defined as the Doppler analysis volume minus the volume of the eye (16 km < radius < 39 km)]. The relatively small volume of strong updrafts may have been the result of the filtering of the updraft magnitudes by the large horizontal scale of the divergence computed from the Doppler analysis.

Peak downdrafts were found inside the radius of maximum wind adjacent to and downwind of the peak updrafts, particularly in the south portion of the eyewall in Figs. 7a–d. South and east of the storm center the downdraft peaks were located downwind of the reflectivity maximum in the southwest portion of the eyewall. The magnitudes of the peak downdrafts estimated by the Doppler analysis were slightly greater than the cores in the upper 10% of the population described by Jorgensen et al. (1985). The strongest downdrafts, about -5 m s^{-1}, were observed at 3- and 6-km altitude (Figs. 7b and 7c), radially inward from the peak updrafts.

The volume of the eyewall region covered by downdrafts less than -1 m s^{-1} ($\sim$12%) was comparable with that presented by Jorgensen et al. (1985). The largest region of downdrafts less than -1 m s^{-1} was at 3-km altitude (Fig. 7b), with an extensive region of downward motion in the southeast portion of the eyewall, downwind from the area of strong reflectivity. Relatively large areas (9–12 km^2) with downdrafts less than -3 m s^{-1} were observed up to 9-km altitude along the inside edge of the eyewall, suggesting large amounts of subsiding air along the inside edge of the eyewall. Black and Hallett (1986) suggested that the occurrence of these downdrafts indicated substantial mixing between the saturated air of the eyewall and the drier, subsiding air of the eye. The mixing could give rise to some slight negative buoyancy, further strengthening the downdrafts. Regions with downdrafts of comparable magnitude and size were also observed on the southeast side of the eyewall in Figs. 7a and 7b, downwind of the reflectivity maximum.

b. Azimuth–height cross sections

Azimuth–height plots at constant radius depict the asymmetric structure of the wind and reflectivity fields with respect to the storm track. The cross sections in Fig. 8 are for 26-km radius (close to the radius of maximum wind). These sections are centered on the direction (327°) toward which the storm was moving. To the left of the track the tangential wind maximum was found at 1 km at azimuth 230° (Fig. 8a). From there it sloped upwind (to the right) to 3 km at azimuth 40°, where it remained nearly constant in altitude to the rear of the storm. To the left of track and the rear of the storm, the tangential wind maximum was very shallow, decreasing very rapidly with increasing altitude. On the right side and in front of the storm, the tangential wind maximum was relatively deep, decreasing only slightly with increasing altitude up to 5 km. Above 7 km the vertical gradient was comparable on both sides of the track.

Figure 8b shows that below 2-km altitude the radial wind was characterized by inflow in front of the storm (327° azimuth) and outflow behind. This inflow–outflow pattern is consistent with the theoretical results of Shapiro (1983). In his example of a slow-moving storm (velocity < 5 m s^{-1}), the maximum inflow occurred within the eyewall region, ahead of the storm, and the maximum outflow at the rear. Marks and Houze (1987) found that in Hurricane Alicia this inflow–outflow asymmetry extended to higher altitudes. This was not the case in Norbert. At 3.5 km (Figs. 8b and 6b), the air motion was nearly circular and fairly symmetric. At levels higher than 3 km the air motion was more asymmetric. The pattern in the radial flow switched to a deep layer of inflow from the rear of the storm and a comparably deep layer of outflow in the front—a reverse of that at 1 km. The vertical transition from inflow to outflow thus occurred in the same altitude interval that the tangential wind maximum switched from the left to the right of track, suggesting that there was strong shear in the flow in which the vortex is embedded.

Figure 8c shows that the vertical velocity maximum at this radius was to the left of the storm track at all levels. The maximum sloped upward and downwind, along the upper boundary of the reflectivity maximum, from ahead of and just to the left of the storm center at 2.5-km altitude to behind and to the left of the storm center at 9-km altitude. There was a weaker, secondary

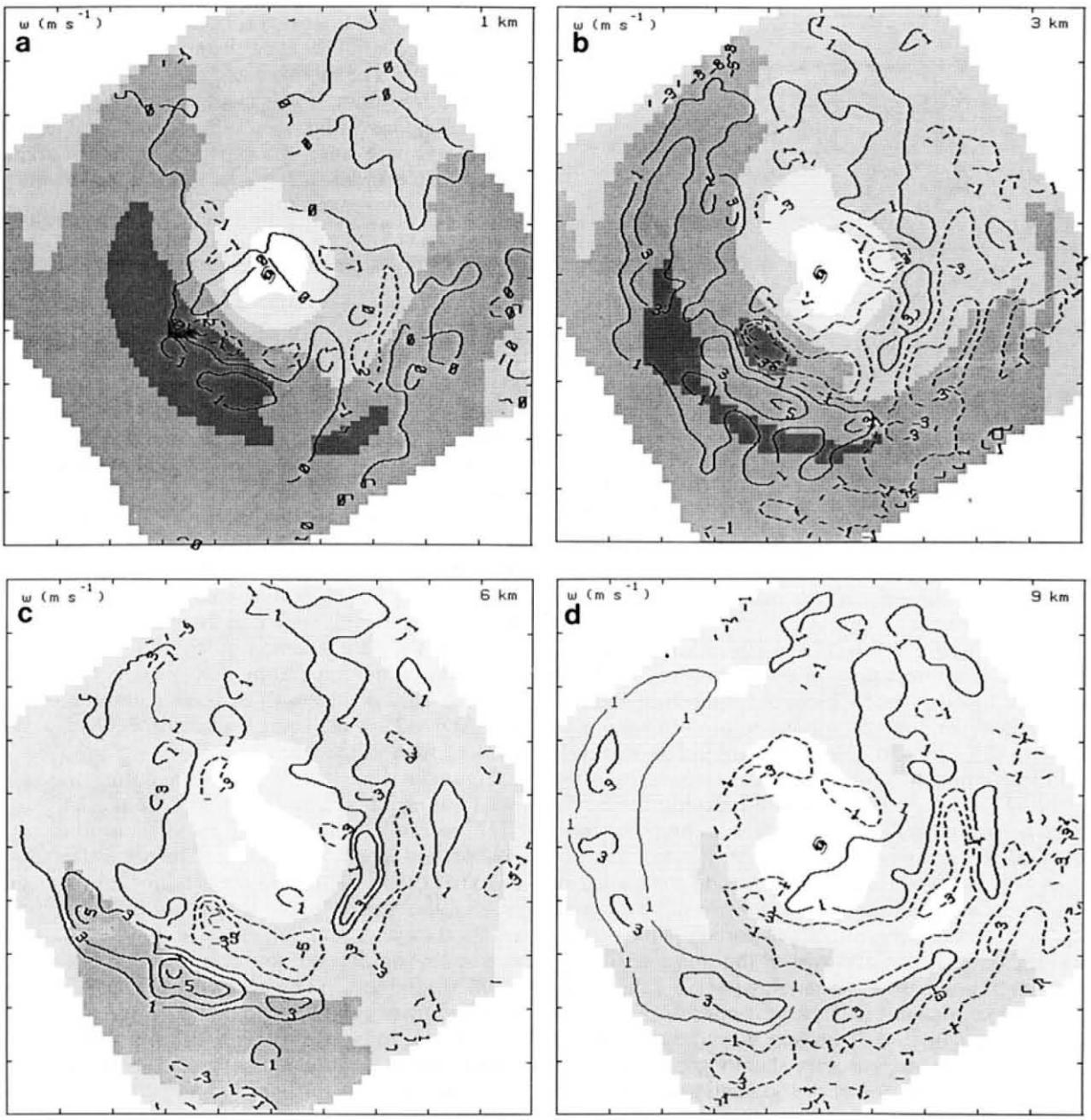

FIG. 7. As in Fig. 6 but for the Doppler-derived vertical velocity (m s^{-1}). Vertical velocity is depicted using contours, where positive values are indicated by solid lines and negative values by dashed lines.

maximum to the right of the storm track at 4-km altitude (27° azimuth). Downwind of the primary maximum, in the right-rear quadrant of the storm (120°–150° azimuth), was a large region of downward motion centered at 3- to 4-km altitude. In the vicinity of the reflectivity maximum the vertical velocity was near zero, with a few isolated areas of downward motion. Above 7 km there was positive vertical motion at most azimuths.

The inflow–outflow pattern in the radial wind evident in Fig. 8b was seen at other radii, with a slight variation in magnitude, which peaked just outside the radius of maximum wind, decreasing both inward and outward from there. The azimuth–height structure of the tangential and vertical wind components varied strongly with radius. In Fig. 9, azimuth–height cross sections of the streamlines and isotachs of the tangential-vertical flow at constant radius for 16, 26, and 36 km graphically depict this variability. Figure 9b shows again the position of the tangential wind maximum sloping upwind from a position to the left of track below 2-km altitude to a position to the right of track at 3

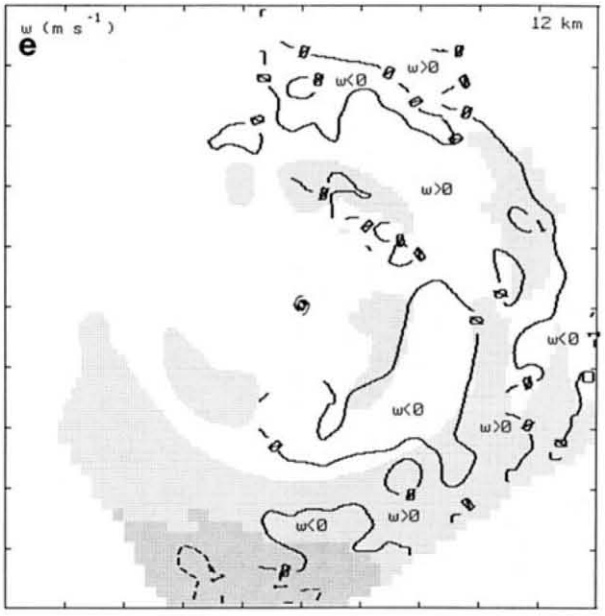

FIG. 7. (*Continued*)

km. Examination of Figs. 9a–c shows that the position of the maximum tangential wind sloped upwind with increasing radius, as well as altitude, from 0.5-km altitude and 210° azimuth at 16-km radius to 1.0-km altitude and 215° azimuth at 26-km radius to 3.5-km altitude and 55° azimuth at 36-km radius. The slope was larger outside the radius of maximum wind.

The steep upward slope with azimuth of the streamlines to the left of the track at 26 km (Fig. 9b) indicated the position of the peak updraft shown in Fig. 8c. The streamlines at 36 km (Fig. 9c) were less steeply sloped with azimuth (more stratiform) than at 16 and 26 km (Figs. 9a and 9b). Inside the eyewall (Fig. 9a) the slope of the streamlines was sharply downward in the reflectivity maximum at 200° and upward in the right-rear quadrant of the storm downwind of the reflectivity and tangential wind maxima.

5. Partitioning the relative wind into components

a. Wind partitioning procedure

Observational studies of the kinematic structure of hurricanes have traditionally described only two components of the storm circulation: the axisymmetric mean vortex and the storm motion (e.g., LaSeur and Hawkins 1963; Hawkins and Rubsam 1968; Hawkins and Imbembo 1976), because there were insufficient data to decompose the wind further. Analyses focused on the description of the structure of the mean (axisymmetric) vortex. Because the Doppler analysis provides the first detailed snapshot of the entire three-dimensional wind field in a mature hurricane on a time scale of 1–2 h, it offers an ideal opportunity to describe all of the components of the hurricane circulation, including asymmetries, and to investigate the interaction of the vortex with its environment.

1) DEFINITION OF THE STORM CENTER

Before the wind field can be partitioned, a coordinate system relative to the storm circulation center at all altitudes must defined. A cylindrical coordinate system is used, with a new technique to locate the center of the mean vortex embedded in a mean flow. Earlier techniques have assumed that the center of the storm is exactly vertical. Our method allows the horizontal position of the storm center to vary with height, as it probably does in nature. Thus, the mean vortex is composed of a stack of planes in the vertical, each navigated to a different center, on the assumption that the environmental flow distorted the vortex shape. This procedure prevents the variation in storm center with height from introducing asymmetries into the wind field, which would be the case if the analysis was referred to a common center at all levels (Willoughby 1988).

The center of the storm at each altitude is difficult to determine from the radar since there is no precipitation within the eye, and hence no radar data are actually available in the vicinity of the center of circulation. At each altitude, the Doppler analysis is subjected to the "simplex" algorithm (Neldar and Mead 1965) to find the point that maximizes the tangential circulation within a 10–15-km-wide annulus centered on the observed radius of maximum wind (i.e., the center that had the maximum eyewall vorticity). Figure 10 shows that this center was observed 3–6 km to the right of that determined objectively from the flight-level data (INS position). The mean vortex center, positioned to the right of the storm track, indicated the vortex was moving with a uniform translation velocity. However, the position of the center varied by as much as 3 km with altitude, making an anticyclonic spiral pattern with increasing altitude. This variation of the storm center with altitude suggested that the vortex was embedded in a sheared environment in which the environmental wind veared with height. The small magnitude of the deviation of the center positions with altitude (~3–4 km), however, indicated that on the vortex scale (~100–300 km), the storm center was nearly vertically aligned.

2) DEFINITION OF THE WIND COMPONENTS

In a cylindrical coordinate system centered on the storm, the storm-relative horizontal wind vector can be expressed as

$$\mathbf{v}_r(r, \lambda, z) = \overline{\mathbf{v}_r}(z) + \mathbf{v}'(r, \lambda, z), \qquad (2)$$

where $\overline{\mathbf{v}_r}(z)$ is the horizontally averaged wind vector over a cylindrical portion of the Doppler analysis domain ($A = \pi r_{\max}^2$) centered on the storm,

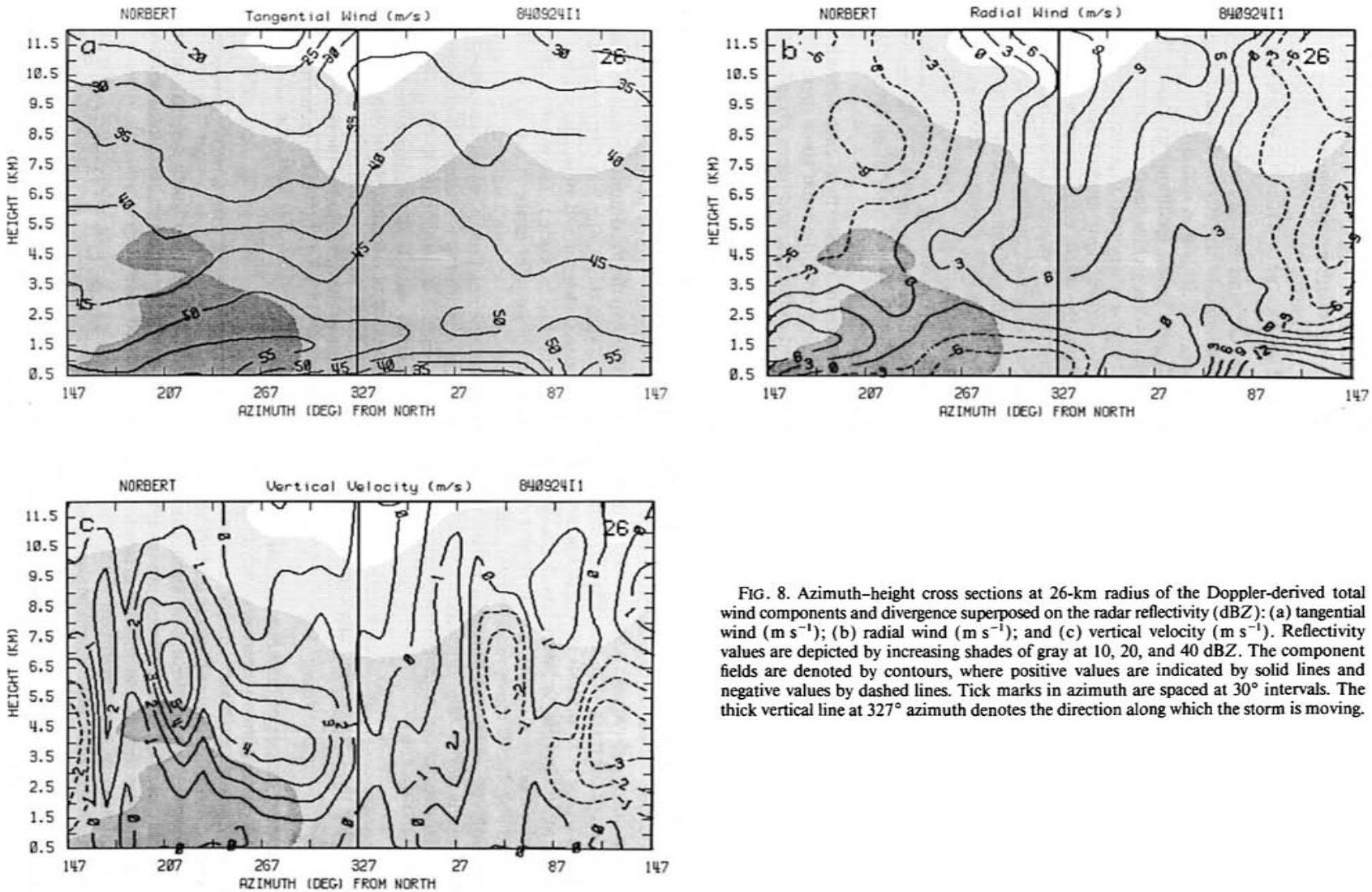

FIG. 8. Azimuth–height cross sections at 26-km radius of the Doppler-derived total wind components and divergence superposed on the radar reflectivity (dBZ): (a) tangential wind (m s^{-1}); (b) radial wind (m s^{-1}); and (c) vertical velocity (m s^{-1}). Reflectivity values are depicted by increasing shades of gray at 10, 20, and 40 dBZ. The component fields are denoted by contours, where positive values are indicated by solid lines and negative values by dashed lines. Tick marks in azimuth are spaced at 30° intervals. The thick vertical line at 327° azimuth denotes the direction along which the storm is moving.

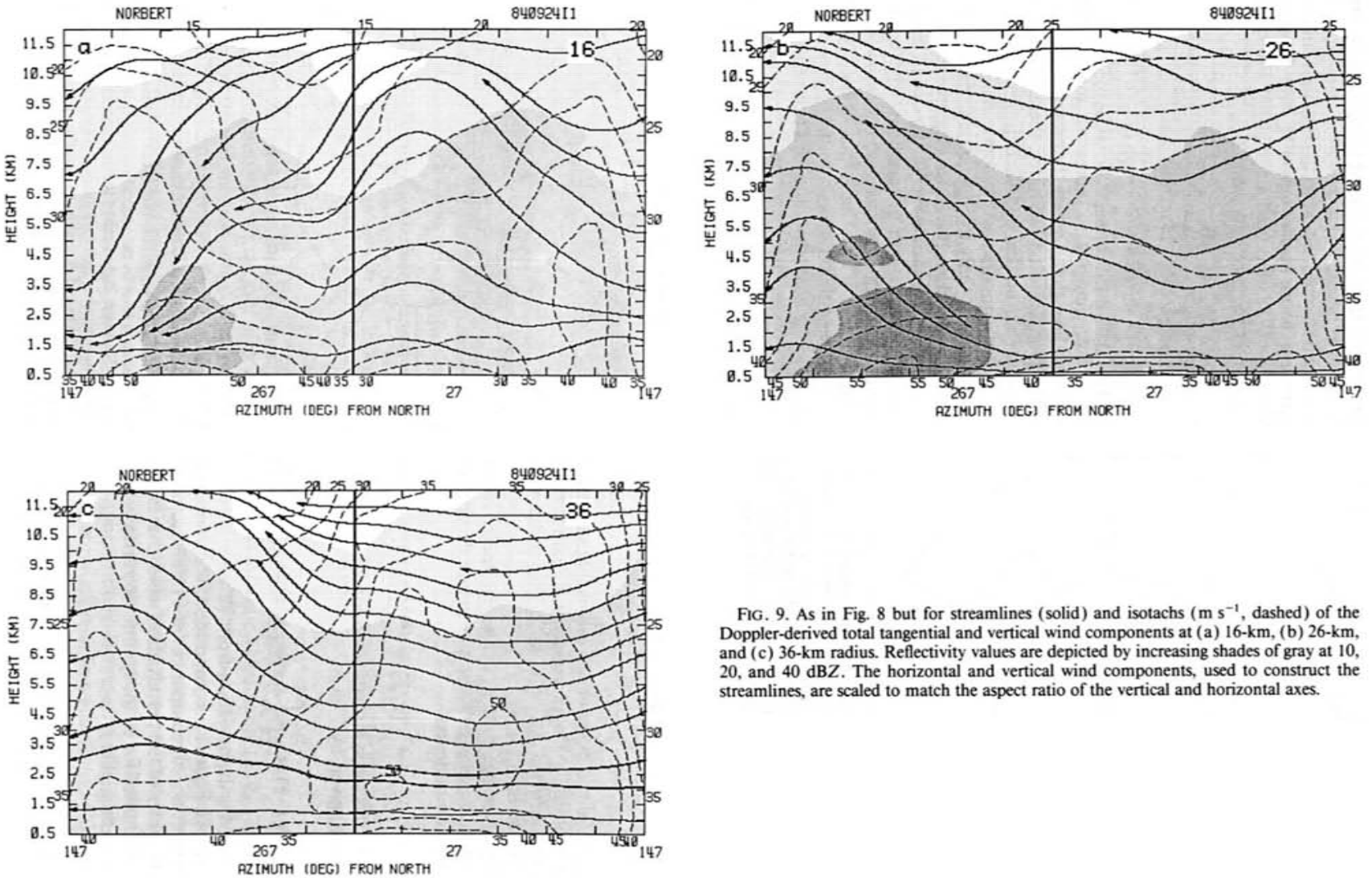

FIG. 9. As in Fig. 8 but for streamlines (solid) and isotachs (m s^{-1}, dashed) of the Doppler-derived total tangential and vertical wind components at (a) 16-km, (b) 26-km, and (c) 36-km radius. Reflectivity values are depicted by increasing shades of gray at 10, 20, and 40 dBZ. The horizontal and vertical wind components, used to construct the streamlines, are scaled to match the aspect ratio of the vertical and horizontal axes.

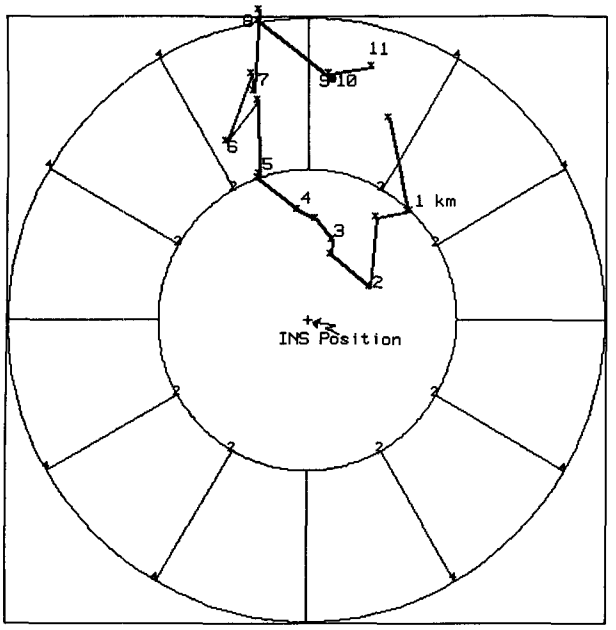

FIG. 10. Position of the symmetric vortex center with altitude relative to the position of the storm center determined from the flight-level inertial navigation system (INS) winds from the aircraft at 3-km altitude. Numbers and asterisks indicate the center position at each 1.0 km and 0.5 km in altitude, respectively, starting at 0.5 km and extending to 11.0 km. Radial distance is denoted by rings at 2- and 4-km radius.

where (i) is the area-averaged storm-relative wind as a function of height, (ii) is the symmetric-vortex (wavenumber 0) circulation, and (iii) is the asymmetric perturbation wind (wavenumber 1 and larger). Willoughby (1988) has used a somewhat similar decomposition of the hurricane wind field.

b. *Storm-relative area-averaged wind profile with height*

Figure 11 shows a hodograph of $\overline{\mathbf{v}}_r(z)$ computed using (3). The mean wind was west to northwesterly below 3 km, changing to increasing southeasterly and southerly flow aloft. Despite the presence of small biases in the Doppler wind estimates, the analysis evidently included information on the environmental flow. Figure 11 was compared with synoptic analyses as a means of verification. Only the operational 200 hPa and gradient-wind level analyses were available for this region. The mean wind profile in Fig. 11 was in good qualitative agreement with the gradient-wind level (~1.5 km) analysis, which showed weak northwesterly flow along the coast of Baja California. At the 200-hPa level (~9–10 km) the flow was southerly as a trough approached the coast from the west (Gunther and Cross 1985).

The mean wind was closest to the storm motion at 3–4-km altitude, indicating that below this level, the

$$\overline{\mathbf{v}}_r(z) \equiv \frac{1}{2\pi}\int_0^{2\pi}\int_0^{r_{\max}} \mathbf{v}(r, \lambda, z)\,dr d\lambda. \qquad (3)$$

Here $r_{\max}$ is defined as the largest radius that surrounds the center within the Doppler analysis domain at every level in the vertical ($r_{\max}$ = 37 km). The vector $\mathbf{v}'(r, \lambda, z)$ is the deviation from $\overline{\mathbf{v}}_r(z)$.

Taking advantage of the circular symmetry of the horizontal-storm wind field, we may in turn decompose $\mathbf{v}'$ into two components:

$$\mathbf{v}'(r, \lambda, z) = \tilde{\mathbf{v}}'(r, z) + \mathbf{v}^*(r, \lambda, z), \qquad (4)$$

where $\tilde{\mathbf{v}}'(r, z)$ is the symmetric component of the hurricane vortex, given by

$$\tilde{\mathbf{v}}'(r, z) \equiv \frac{1}{2\pi}\int_0^{2\pi} \mathbf{v}'(r, \lambda, z)\,d\lambda, \qquad (5)$$

and $\mathbf{v}^*(r, \lambda, z)$, the deviation from $\tilde{\mathbf{v}}'$.

In terms of a Fourier decomposition, $\tilde{\mathbf{v}}'$ corresponds to the wavenumber 0 component of $\mathbf{v}'$. The vector $\mathbf{v}^*$ is the remainder of the perturbation wind; that is, the part not accounted for by the symmetric vortex (wavenumbers 1 and higher).

Equation (2) can now be written as

$$\mathbf{v}_r(r, \lambda, z) = \overline{\mathbf{v}}_r(z) + \tilde{\mathbf{v}}'(r, z) + \mathbf{v}^*(r, \lambda, z), \qquad (6)$$
$$\text{(i)} \qquad \text{(ii)} \qquad \text{(iii)}$$

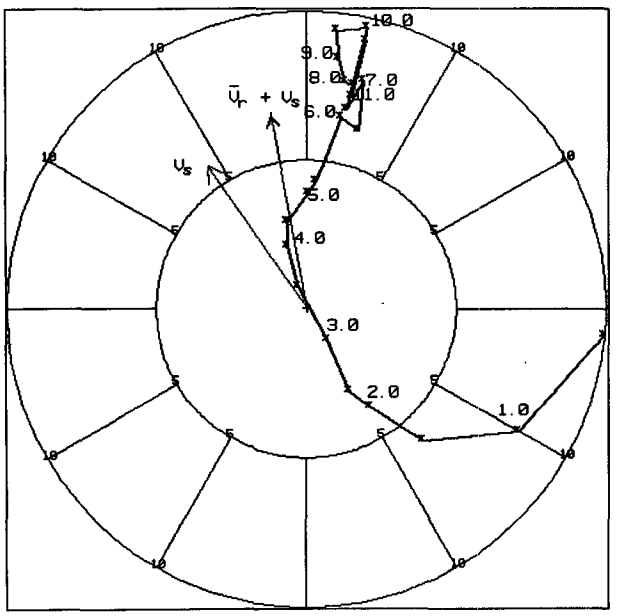

FIG. 11. Hodograph of the mean relative horizontal wind $[\overline{\mathbf{v}}_r(z)]$ at each level in the vertical derived from the Doppler wind analysis. Numbers and asterisks indicate speed and direction of the relative mean wind at each 1.0 km and 0.5 km in altitude, respectively, starting at 0.5 km and extending to 11.0 km. The arrow ($\mathbf{v}_s$) indicates the storm motion during this time, and the arrow ($\overline{\mathbf{V}}_r + \mathbf{v}_s$) the mass-weighted deep-layer mean wind from the Doppler analysis. Velocity intervals are denoted by rings at 5 and 10 m s^{-1}.

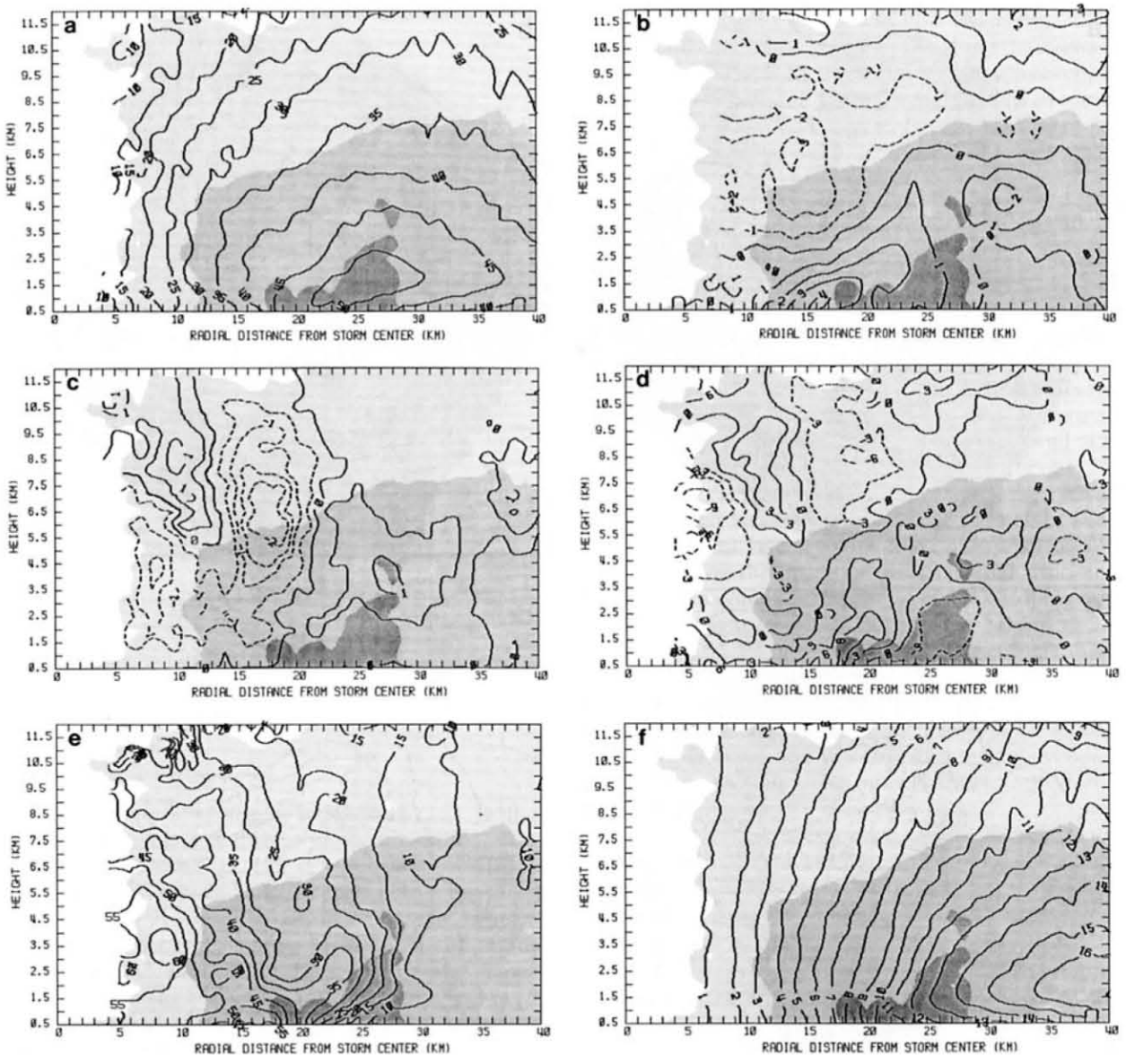

FIG. 12. Radius–height cross sections of the symmetric (azimuthal) mean Doppler-derived fields superposed over radar reflectivity (dBZ): (a) tangential wind (m s^{-1}); (b) radial wind (m s^{-1}); (c) vertical velocity (m s^{-1}); (d) divergence (10^{-4} s^{-1}); (e) vorticity (10^{-4} s^{-1}); and (f) absolute angular momentum (10^5 m^2 s^{-1}). Variables are depicted as in Fig. 8. The vertical velocity in (c) is contoured in 0.5 m s^{-1} intervals. Reflectivity values are depicted by increasing shades of gray at 10, 25, and 38 dBZ.

storm was moving faster than its environment and drawing in the environmental air in front of it. Above this level, the storm was moving slower than its environment, with the environmental air entering at the back of the storm. This inference is consistent with the azimuthal cross section of radial wind shown in Fig. 8b.

In many earlier studies, tropical cyclones were considered to move as a point vortex in a uniform, noninteracting fluid flow. That is, the storm moves with the speed and direction of a deep-layer mean environmental flow. Such a "steering" concept accounts for 30%–80% of the variability of the 24–72-h storm motion in the Atlantic (Neumann 1979). There is considerable uncertainty as to the atmospheric level or layer that determines the storm motion (e.g., Dong and Neumann 1986). Past studies by Neumann (1979) and Pike (1985, 1987) demonstrated the higher correlation of storm displacement with the flow at midtropospheric levels. However, both studies showed the highest correlation with a mass-weighted, deep-layer mean flow.

Figure 11 shows that the vertical, mass-weighted average of the mean horizontal wind throughout the

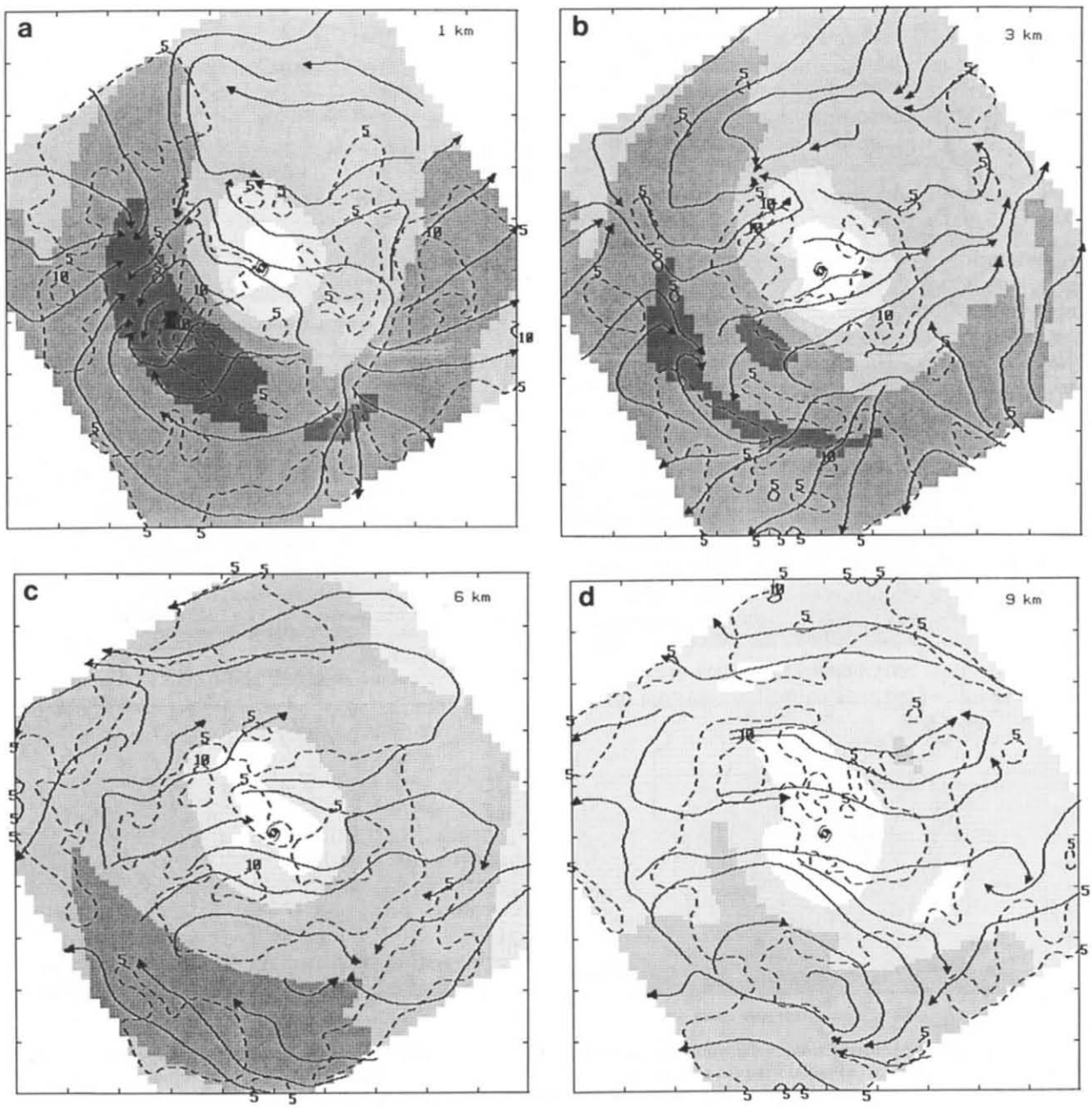

FIG. 13. As in Fig. 6 but for the asymmetric perturbation wind field, $\mathbf{v}^*$ (streamlines and isotachs, m s^{-1}) at altitudes (a) 1, (b) 3, (c) 6, (d) 9, and (e) 12 km.

depth of the analysis ($\bar{\mathbf{V}} + \mathbf{v}_s = 162°$ at 5.8 m s^{-1}) was nearly identical to the storm motion ($\mathbf{v}_s$) in speed and 15° to the right of the storm track. Similar deviations of the storm motion from the mean flow have been described in a number of studies (e.g., George and Gray 1976; Chan and Gray 1982; Holland 1984; Dong and Neumann 1986). These studies indicate that storms tracking toward the northwest tend to move faster than, and 10°–20° to the left of, the mean flow. The deviation from the mean flow is attributed to advection of storm scale as well as the earth's vorticity (e.g., DeMaria 1985; Chan and Williams 1987). Willoughby (1988) described this deviation as the cross-vortex flow that arises from the movement of the vortex through the environmental current. However, from the discussion in section 3c on the accuracy of the Doppler winds, it was possible that part of the observed deviation was a result of overestimating the westerly wind components in the Doppler analysis (3.6 m s^{-1} at 3 km and 3.5 m s^{-1} at 6 km). Subtraction of a westerly bias of 3.0–3.5 m s^{-1} from $\bar{\mathbf{V}}$ resulted in the storm moving slightly to the right of the deep-layer mean. The deep-layer–

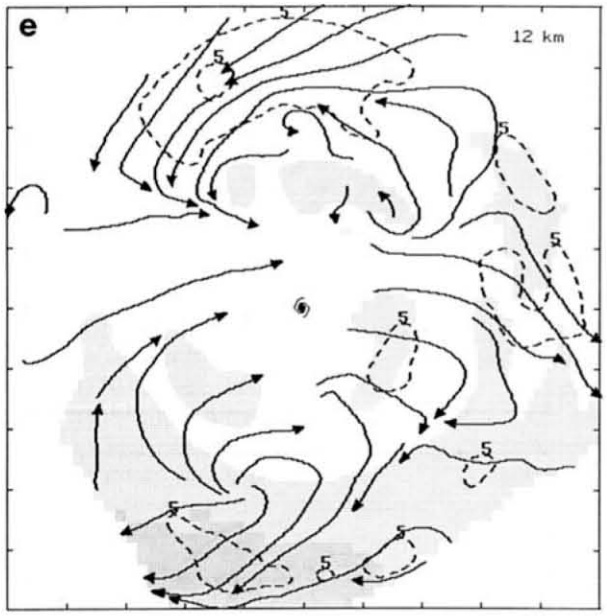

FIG. 13. (*Continued*)

mean deviation in Norbert therefore cannot be resolved in the absence of independent estimates of the mean wind at levels other than 3 and 6 km.

c. *Symmetric vortex*

The symmetric vortex ($\tilde{v}'$), defined by (5), is illustrated in Fig. 12. The three components of the vector field are shown in Figs. 12a–c, while its associated divergence, vorticity, and angular momentum are shown in Figs. 12d–f. It is useful to compare these fields, which represent a decaying storm, to those of the mature Hurricane Alicia described by Marks and Houze (1987). The tangential wind maximum in Fig. 12a (52 m s^{-1}, centered at 26-km radius and 1.5-km altitude) was shallower and extended over a broader radial band than that observed in Alicia (cf. Fig. 7 in Marks and Houze 1987). However, as in Alicia, the wind maximum sloped outward with height (at an angle of 60° from the horizontal), and the wind and reflectivity maxima were nearly collocated in radius.

Unlike in Alicia, the radial wind (Fig. 12b) is weak over most of the inner core, with a mean value near zero. Below 5-km altitude there was a narrow band of outflow of 1–3 m s^{-1} (peak of 4 m s^{-1} at 16-km radius and 1.0-km altitude) along the inside of the tangential wind and the reflectivity maxima from 1.5–6.0-km altitude. From 5 to 9 km the radial flow was weakly inward, and above 9 km it was outward. This mean radial flow pattern in Norbert is somewhat similar to that in "Box 2" of Alicia (cf. Fig. 8b in Marks and Houze 1987), which encompassed the rear portion of the eyewall and also had a stratified structure of alternating inflow and outflow regions with altitude. This portion of Alicia's eyewall was also characterized by weaker tangential flow and updrafts along the eyewall. The similarity between the radial flow in a weakening storm like Norbert and the weaker quadrant of a mature storm such as Alicia suggests that this layered radial wind structure may be characteristic of weak or weakening storms.

The major differences between the tangential and radial flow in Alicia and Norbert were probably related to the tendency in the storm intensity. Alicia, at the time of the Doppler analysis, was weaker than Norbert (967 hPa central pressure versus 952 hPa). However, Alicia was quite mature and even slowly intensifying, while Norbert had begun to fill.

The symmetric mean fields of the vertical velocity, divergence, vorticity, and angular momentum are all consistent with the fact that Norbert's eyewall was weakening. The azimuthal mean w field (Fig. 12c) showed that the mean vertical velocities in the eyewall were extremely weak. There were two channels of weak upward vertical velocity with maxima of $\sim$1 m s^{-1}. One was along the inside of the tangential wind and reflectivity maxima (peak w = 1.4 m s^{-1}), sloping outward with height from 22-km radius at 2.0-km to 33-km radius at 6.5 km ($\sim$67° from the vertical). This slope of the w maximum paralleled the slopes of the radial velocity outflow and the tangential-velocity maxima. The second maximum (peak w = 1.1 m s^{-1}) was nearly vertical and was centered at 11-km radius above 5-km altitude. The outer w maximum corresponded to the primary eyewall, while the inner maximum apparently corresponded to the remains of the inner eyewall. Downward motion dominated the radii inward from 20-km radius, with a peak downdraft of -2.2 m s^{-1} at 18-km radius and 6-km altitude, just inside the primary eyewall.

Figure 12d shows that the only boundary-layer convergence in the azimuthal mean was centered at the radius of the maximum wind. Inside that radius there was mean boundary-layer divergence. Above the boundary layer, divergence predominated in the eyewall region, and convergence predominated in the eye (radius < 18 km). The only significant feature in the divergence field above the boundary layer was a narrow channel (3 km wide) of enhanced divergence (3–6 $\times 10^{-4}$ s^{-1}). This maximum sloped outward with increasing radius along the outer eyewall wind maximum in association with the primary eyewall updraft.

The azimuthal mean vorticity, shown in Fig. 12e, was still relatively strong, with a peak value of 6.2 $\times 10^{-3}$ s^{-1} (comparable with those reported from composite analyses of flight-level data) at 9-km radius and 3-km altitude. A secondary peak of 3.6 $\times 10^{-3}$ s^{-1}, corresponding to the shallow tangential wind maximum in the primary eyewall, was at 23-km and 2-km altitude. The presence of two vorticity maxima suggests that the inner eyewall, evident in the radar data from the previous two days, had not spun down completely.

The vorticity associated with the inner eyewall was actually stronger and extended to a greater depth than that of the outer eyewall (7.5 km versus 5.0 km), suggesting this inner eyewall contained more vigorous convection during its evolution. Either the inner eyewall took longer to spin down than the decay of the inner eyewall reflectivity maximum indicated, or it was characterized by periodic bursts of deep convection that maintained its intensity. The complete ring of maximum reflectivity had disappeared almost 2 days earlier. However, a partial ring of reflectivity and an inner secondary wind maxima, presumed to be the remains of the old inner eyewall, were clearly present during the flights on the second and third day.

The azimuthal-mean absolute angular momentum (M), defined as in Hawkins and Rubsam (1968), is

$$M = v_\theta r + \frac{fr^2}{2}, \tag{7}$$

where r is radius from the storm center, v_θ is the tangential component of $\tilde{\mathbf{v}}'$, and f is the Coriolis parameter, also showed that the inner eyewall was still intense (Fig. 12f). The M surfaces were nearly vertical at radii < 20 km. At radii > 20 km, the M surfaces sloped outward with altitude above 2 km. The M surfaces associated with each eyewall thus had slopes comparable with the corresponding vertical velocity maxima. The slope of the M surfaces in the outer eyewall was less steep and extended over a shallower layer than the inner eyewall. Below 2-km altitude the M surfaces sloped outward with decreasing altitude, indicating momentum loss to friction in the inflow layer. The shape of the M surfaces and their slope relative to the updrafts were similar to corresponding features described by Emanuel (1986) and Rotunno and Emanuel (1987) in their studies of steady-state hurricane structure. Hence, the secondary circulation apparently was still working to maintain the vortex, while other mechanisms were acting gradually to spin down the vortex.

d. Asymmetric structure

Figure 13 shows the $\mathbf{v}^*$ field at altitudes of 1, 3, 6, 9, and 12 km. Two basic types of $\mathbf{v}^*$ flow are evident in Fig. 13: 1) a source–sink field in close proximity to each other aligned along the axis of the storm motion at 1 km (Fig. 13a compared with Fig. 14a) and 2) a vortex couplet embedded in flow along the axis of storm motion at 3, 6, 9, and 12 km (Figs. 13b–e compared to Fig. 14b). The source–sink field was evident at altitudes below 3 km, where the storm motion was opposite to and stronger than the horizontal mean flow [$\overline{v}_r(z)$]. The source and sink were centered at the radius of maximum wind (~26 km). The sink was located northwest of the storm center, in the region of maximum inflow and upward motion at this altitude in the eyewall, while the source was southeast of the center in the region of maximum outflow and downward motion (cf. Fig. 8). The flow across the storm center was from the southeast, parallel to the storm motion.

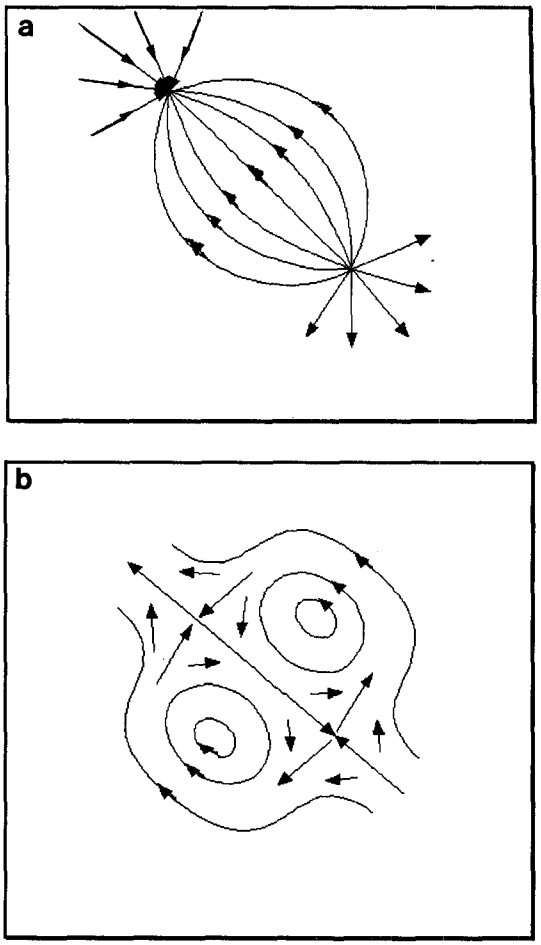

FIG. 14. Schematic representation of (a) a source–sink pair embedded in a northwesterly mean flow and (b) a vortex couplet embedded in a southeasterly mean flow.

At altitudes > 3 km, where $\overline{v}_r(z)$ was parallel to and greater than the storm motion, the $\mathbf{v}^*$ field was characterized by a wavenumber 1 cyclonic/anticyclonic eddy couplet that was centered on the radius of maximum wind (~26 km). The cyclonic eddy was located in the right front quadrant of the storm (north, northeast), and the anticyclonic eddy was located in the left rear quadrant of the storm (south, southwest). The flow between the eddies was from the west, as opposed to that outside the eyewall, which was nearly parallel to the motion of the storm. This flow pattern was reminiscent of flow around an obstacle. There was a "stagnation point" on the southeast side of the storm, where the flow separated around the eyewall, and a col on the northwest side of the storm, where the flow returned to the direction it had before encountering the eyewall. This pattern was most evident at 6 and 9 km, where the radius of maximum wind was well within the analysis domain (Figs. 13c–d). At 12 km (Fig. 13e) the

eyewall filled the whole analysis domain and the flow surrounding the eyewall was not observed. At 3 km (Fig. 13b) the col northwest of the center was at the edge of the analysis domain, and the return to southeasterly flow was not evident.

The eddies observed in Figs. 13b–e are much smaller in scale than large-scale gyres discussed by Willoughby (1988) and Fiorino and Elsberry (1989). The small-scale eddies or gyres that we observed are contained entirely within the inner-core region of the storm, centered at the radius of maximum wind. They may have been a result of a nonlinear interaction between the mean vortex and the storm motion. Peng and Williams (1990) have described such interaction in their recent analytical and numerical studies of the motion of a shallow-water barotropic vortex. Their model produced two different waves with wavenumber 1 asymmetry: an inner gyre centered on the radius of maximum wind associated with a linear instability of the mean vortex and large-scale outer gyres. The outer gyres correspond to those of Willoughby (1988) and Fiorino and Elsberry (1989), while the inner gyres, corresponding to those seen in Fig. 13, resulted from barotropic instability of the vortex. The position of the gyres in Figs. 13b–d is in agreement with the results of Peng and Williams (1990). Although the horizontal flow varied with altitude, the small-scale gyres were nearly aligned in the vertical, suggesting the instability extended throughout the depth of the vortex above the boundary layer.

The reversal in the inflow–outflow pattern with height shown in Fig. 8b can be understood through a linear combination of the two asymmetric components in (6); that is, $\overline{v}_r(z) + v^*$. Figure 15 shows that these components dominated the radial component of the mean vortex at the radius of maximum wind. At 1 km, $\overline{v}_r$ dominated v^*, and the total flow consisted of strong

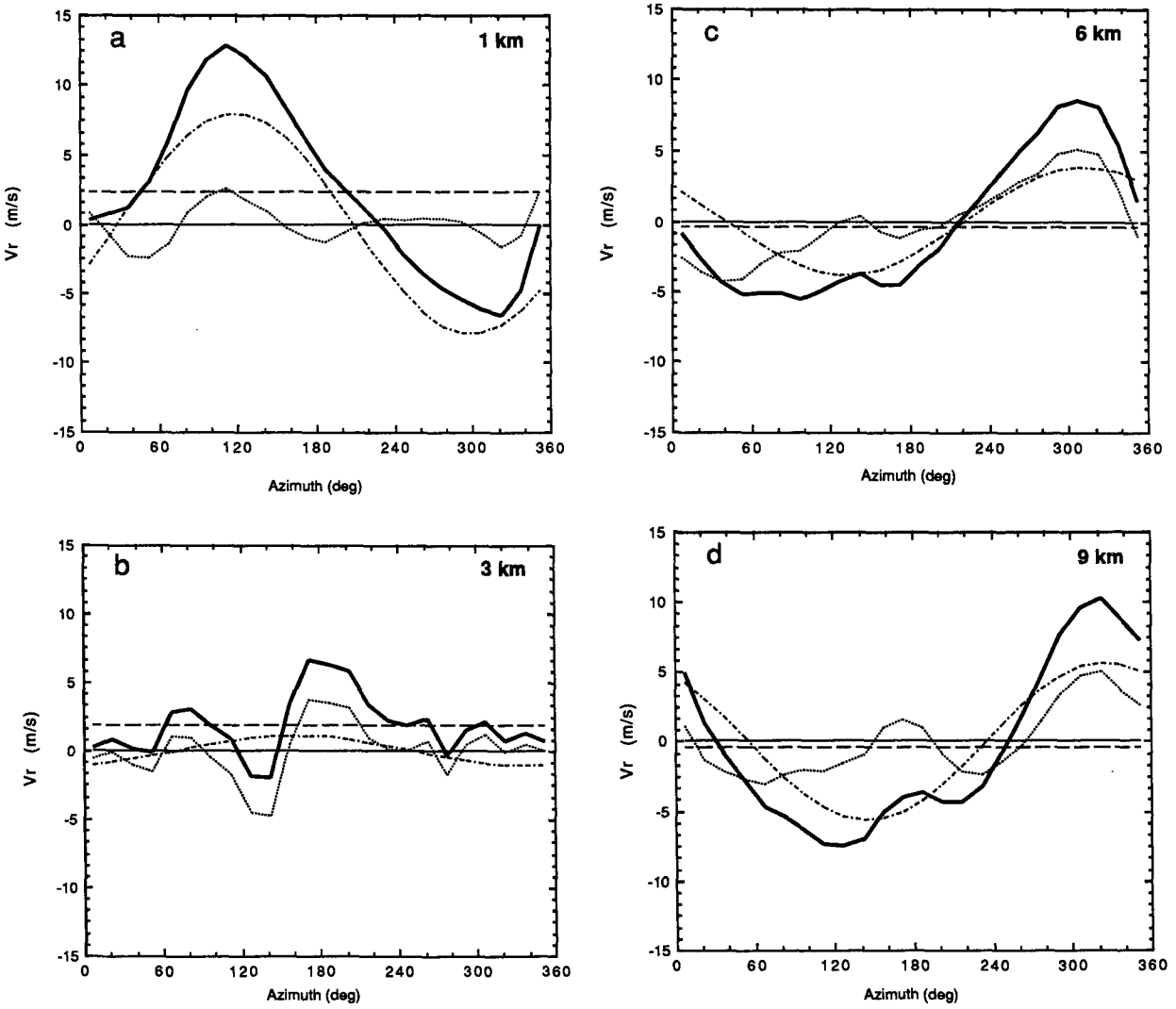

FIG. 15. Azimuthal variation of the magnitude of the radial component of $\overline{v}_r(z)$ (dot–dash line), v^* (dotted line), $\tilde{v}'$ (dash line), and v_r (solid line) at 26-km radius and (a) 1, (b) 3, (c) 6, and (d) 9 km.

inflow in the front of the storm, strong outflow behind, and much of the air passing around the storm. At 3 km the magnitude of $\overline{v_r}$ was less than v^* and the gyres began to dominate the radial flow, resulting in the reversal of the radial flow asymmetry observed in Fig. 8. At 6, 9, and 12 km $\overline{v_r}$ and v^* were nearly equal in magnitude, and inflow remained in the rear of the storm. The axis of the v^* field was nearly parallel to the $\overline{v_r}(z)$ shear vector between 1 and 11 km, resulting in little variation in azimuth of the inflow–outflow axis with height.

As pointed out in section 4, the divergence and vertical velocity patterns were asymmetric, and the only asymmetries in the wind field were associated with $\overline{v_r}(z)$ and v^*. The upward motion, which starts at low levels in front of the storm and curves upward to the rear of the storm, and the downward motion concentrated at low levels in the rear and right side of the storm (Figs. 8c–d) can thus be understood in terms of the divergence of $\overline{v_r}(z)$ and v^*.

The preceding discussion points to possible answers to important questions related to storm motion, intensity change, and interaction of the vortex with its environment. Since the linear combination of the mean horizontal flow and the inner gyres determines the location of the updrafts and downdrafts in the eyewall, changes in either one can effect the location of the updrafts and downdrafts and thus alter the storm structure and intensity. If the recent studies by Willoughby (1988) and Fiorino and Elsberry (1989) are correct in that the mean horizontal flow (large-scale outer gyres) changes with time over a storm's track, these changes could affect the storm intensity. If, as proposed by Peng and Williams (1990), the inner gyres are instabilities of the mean vortex that also change over the storm's lifetime, these changes could also affect storm intensity. The instability causing the inner gyres may thus be dependent upon changes in the mean horizontal flow or outer gyres. Observational and theoretical experiments will be needed to address these questions.

6. Trajectory analysis

Air parcel trajectories entering the eyewall updraft were derived from the Doppler wind field. They were calculated in storm-relative coordinates on the assumption that the wind field and the mean storm motion were in steady state. Under these assumptions, the air parcel position at any time (t_n) after the initial time (t_0) can be expressed as

$$x_n = x_{n-1} + (u - c_x)(dt) \quad (8a)$$

$$y_n = y_{n-1} + (v - c_y)(dt) \quad (8b)$$

$$z_n = z_{n-1} + (w)(dt), \quad (8c)$$

where $(x_{n-1}, y_{n-1}, z_{n-1})$ is the location of the trajectory at t_{n-1} [when $n - 1 = 0$, (x_0, y_0, z_0) is the location of the starting point for the trajectory]; (x_n, y_n, z_n) is the location of the trajectory at t_n; (u, v, w) are the wind components from the Doppler analysis at $(x_{n-1}, y_{n-1}, z_{n-1}, t_{n-1})$; (c_x, c_y) is the mean storm motion from the computed track; and $dt = t_n - t_{n-1}$ (30 s was used). The scale of the Doppler analysis grid is such that the computed trajectories best represent the mesoscale motion of air parcels. The actual air trajectories probably deviated from those computed by (8); however, the computed trajectories should characterize the general shape and position of the majority of possible air parcel motions.

Trajectories were computed for 60 initial points (x_0, y_0, z_0). However, very few trajectories entered the updraft region on the left side of the track. Those that did not spiraled around the center, eventually leaving the analysis domain. The only trajectories to enter the updraft started in two primary locations: 1) along the inside edge of the northwest eyewall and 2) in the northeast quadrant of the storm outside the eyewall. Figure 16 shows these trajectories.

The trajectory in Fig. 16a, starting along the inside of the eyewall, began at an altitude of 1.1 km in the vicinity of the region of maximum convergence in the front of the storm. It spiraled slowly upward and outward, moving around the storm twice before entering the base of the principal updraft region. Passing through the updraft region, it climbed from 2.3-km altitude to near 8 km, the outflow level, in 0.5 h. After reaching the 8.0-km level southeast of the center, the parcel continued to spiral outward, climbing slowly to 11.3-km altitude, making one more circuit of the storm. Trajectories started at other locations along the inside edge of the eyewall descended to the surface before making one circuit of the storm or missed entering the updraft and spiraled slowly out of the analysis domain.

The second updraft trajectory started at the edge of the analysis domain in the right-front quadrant of the storm at an altitude of 2.0 km (Figs. 16b and 17). Trajectories starting in this region entered the updraft region on the first circuit of the storm, or missed it and spiraled slowly out of the analysis domain, never entering the eyewall circulation. The trajectory in Fig. 16b entered the updraft region at the same point as the trajectory in Fig. 16a, following a nearly identical track through the outflow layer.

Figure 17a shows that this trajectory was along the tangential wind maximum as it entered the updraft region. At the entry location the radial flow was strongly inward (Fig. 17b). Comparison of Figs. 17a and 17b shows that the trajectory followed the updraft channel above the tangential wind maximum (roughly paralleling the 40 m s^{-1} isotach) through a narrow region of outflow into the strong inflow layer above 3-km altitude behind the storm (azimuth 109°, time 3512 s). Figures 17a and 17c show that the trajectory was embedded in a region of mesoscale ascent and relatively strong tangential flow as it spiraled outward in the out-

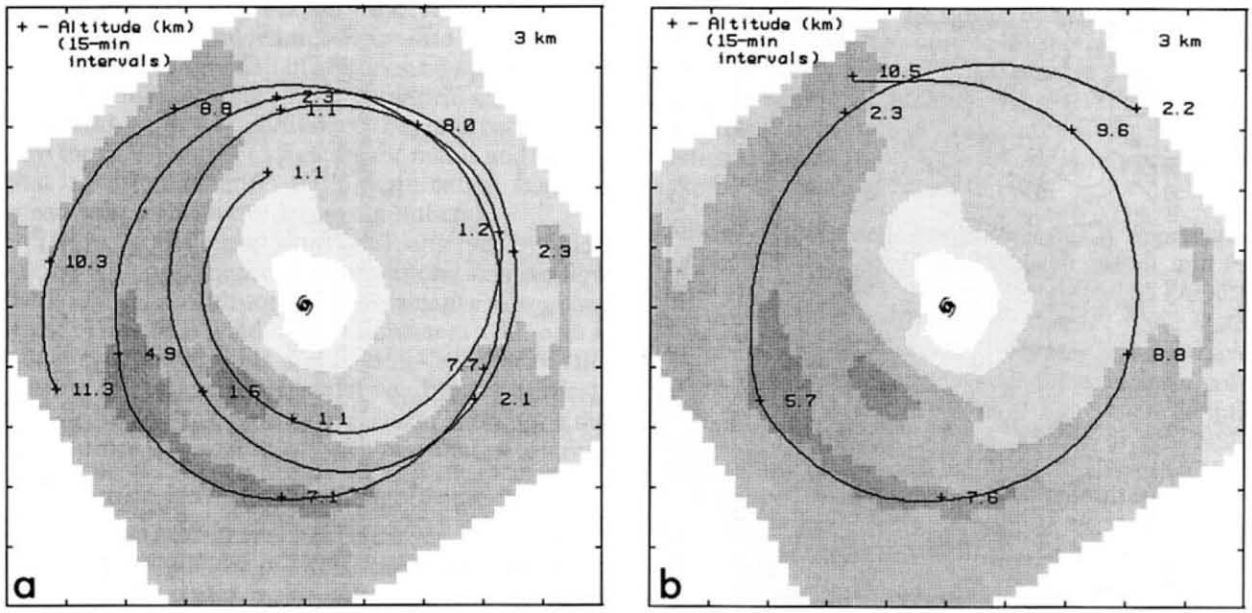

FIG. 16. Plan view of upward mesoscale air trajectories starting (a) inside the eyewall radius and (b) outside the eyewall radius superposed on the reflectivity (dBZ) at 3-km altitude. The trajectories are denoted by solid lines, where the altitude (km) along the trajectory is indicated by "+" at 15-min intervals. The domain and the reflectivity values are depicted as in Fig. 6.

flow layer. Comparison of Fig. 17a with Fig. 17c suggests that the mesoscale air parcels were transporting tangential momentum upward from the low-level tangential wind maximum on the left of the track to the upper-level maximum on the right of the track.

7. Conclusions

An airborne investigation was carried out on 24–25 September 1984 to study the kinematic structure, physical processes, and scale interactions that were operative in the inner-core circulation of Hurricane Norbert. Both NOAA/AOC WP-3D research aircraft were used. One aircraft, equipped with the airborne Doppler radar, flew repeated radial penetrations in and out of the eyewall, mapping the three-dimensional wind field over the eyewall region. This dataset provides the first complete three-dimensional mapping of the wind field of the hurricane inner core by Doppler radar (or by any means other than compositing of flight-level data from multiple aircraft missions) and a demonstration that the Doppler analysis can be used to deduce the large-scale mean flow, the symmetric vortex structure, and vortex asymmetries.

The three-dimensional wind field within 40 km of the storm center was derived by "pseudo" dual-Doppler synthesis in each quadrant of the storm. The vertical wind components were derived from the mass continuity equation and the horizontal wind field. The Doppler-derived wind fields for the four quadrants were combined to form a storm composite wind field 75 × 75 km on a side, centered on the storm circulation center. The wind field extended from 0.5 to 12.0 km in altitude.

The vertical velocity field deduced kinematically from the horizontal wind analysis is statistically consistent with the flight-level vertical velocity field at the Doppler aircraft flight level as well as at the flight level of the second aircraft (3 km higher in altitude). The horizontal flight-level winds at both altitudes showed point-by-point correlation with the Doppler analysis with a correlation coefficient of 0.98. The vertical velocities that were estimated in the Norbert analysis were much improved over those from the earlier Alicia analysis, primarily because of the shorter time separation between flight legs used for the Doppler analysis.

The Norbert wind field was asymmetric, and the asymmetry varied with altitude. The altitude of the tangential wind maximum sloped upward in the upwind direction. Left of the track (azimuths 147°–327°) it was at 1-km altitude, while to the right of the storm track (azimuths 327°–147°) it was at 3 km. At 1-km altitude, the radial wind was inward in front of the storm (327° azimuth) and outward behind. By 3-km altitude, the radial flow switched to inflow from the rear of the storm and outflow in the front. The vertical velocity maximum was to the left of the storm track at all levels. The maximum sloped upward in the downwind direction and was located along the similarly sloping upper boundary of the reflectivity maximum: from just to the left of the track at 2.5-km altitude to behind and to the left of the storm circulation center at 9-km altitude.

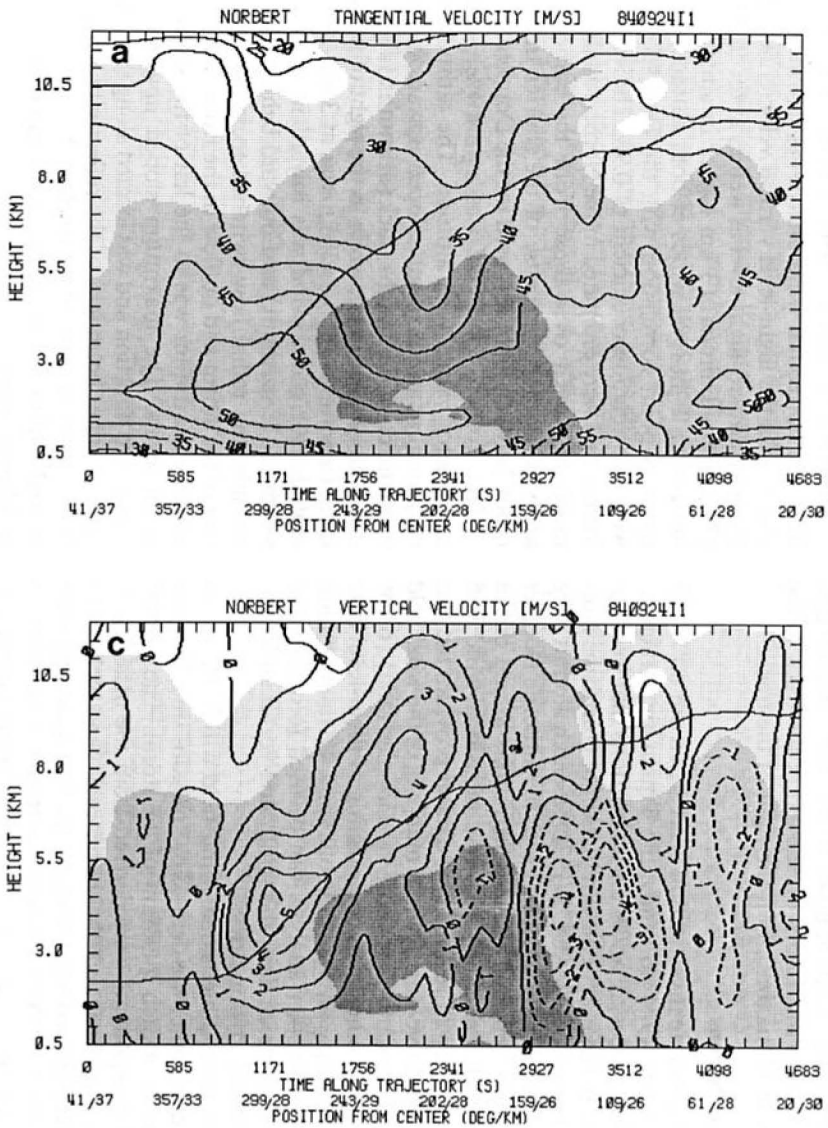

FIG. 17. Vertical cross sections of the mean Doppler-derived wind components (m s^{-1}) superposed on the radar reflectivity (dBZ) along a portion of the trajectory in Fig. 16b. Wind components and reflectivity values are depicted as in Fig. 8. The altitude of the trajectory in the cross section is denoted by the solid black line.

As a means of investigating the nature of the wind field asymmetry, a technique was devised to partition the horizontal wind components into a horizontal mean wind as a function of altitude and a perturbation wind. Taking advantage of the cylindrical nature of the wind field, we further partitioned the perturbation wind into the mean vortex (a function of radius and height, that is, wavenumber 0) and a perturbation from the mean vortex (higher-order wavenumbers).

The horizontal mean wind $\overline{v}_r(z)$, observed by radar, veered with altitude from northwesterly relative flow below 3 km to south-southeasterly relative flow above 3 km. The mean wind was in agreement with operational synoptic analysis and its deep-layer mean (the average of the mean horizontal wind in the vertical) was slightly to the right of the storm motion at the same velocity, in agreement with past studies of storm motion.

The structure of the mean vortex, $\tilde{\mathbf{v}}'$, was similar to that of Alicia and other analyzed storms. However, the mean vortex structure of Norbert differed in ways that indicated the vortex was weakening, that is, broad shallow reflectivity maxima, updraft maximum at low levels, and primarily outflow at all levels.

The perturbation from the mean vortex, $\mathbf{v}^*$, was characterized at lower levels by a sink–source pattern, with the convergent sink on the front, inflow side of the storm and the divergent source on the trailing, outflow side of the inner vortex. At upper levels the perturbation from the mean vortex was characterized by cyclonic and anticyclonic gyres in the right front and left rear quadrant, respectively. The gyres indicate how at upper levels air enters the rear of the storm and flows out the front, in contrast to the low-level inflow–outflow pattern.

The three-dimensional wind structure of Hurricane Norbert documented by airborne Doppler radar will aid our understanding of several aspects of the storm's structure and organization. In Part II, we examine the microphysical structure of the storm in the context of the observed wind pattern. In Part III the thermodynamics of the storm and the storm's water budget will be retrieved from the observed wind pattern.

Beyond these studies of Hurricane Norbert, the present work has significant implications because we have been able to decompose the wind field into four components. We have been able to isolate not only the patterns of radial inflow and outflow associated with the mean vortex, but also the inflow and outflow that result both from the vertical variation of the mean wind $[\overline{v}_r(z)]$ and from horizontal asymmetries of the wind field ($\mathbf{v}^*$). We have seen that both the vertical and horizontal variability contribute significantly to the manner in which air was entering and exiting the vortex. This inflow–outflow pattern is likely crucial to understanding how hurricanes intensify, dissipate, and are maintained in steady state, since it indicates where and how the air of low and high equivalent potential temperature (θ_e) flows in and out of the storm. Since Norbert was a weakening storm, it is of great interest now to apply this technique to an intensifying storm so that the inflow and outflow patterns in the two cases can be compared. Fortunately, a dataset similar to the Norbert set was obtained in the intensifying stages of Hurricane Emily (1987), and work is in progress to make the comparison with Norbert.

Acknowledgments. The authors greatly appreciate the help of R. Burpee, S. Rosenthal, R. Black, and P. Willis. The NOAA Aircraft Operations Center (AOC) operated the aircraft. Without the support of the AOC engineering staff, in particular Terry Schricker, the airborne Doppler radar data would not have been collected. G. C. Gudmundson edited the manuscript. Support was provided to R. A. Houze, Jr., by NSF Grants ATM-8413546 and ATM-8719838 and NOAA Grants 40-WCNR-6-02428 and 40-WCNR-8-06088.

REFERENCES

Black, R. A., and J. Hallett, 1986: Observations of the distribution of ice in hurricanes. *J. Atmos. Sci.*, **43,** 802–822.

Chan, J. C-L., and W. M. Gray, 1982: Tropical cyclone movement and surrounding flow relationships. *Mon. Wea. Rev.*, **110,** 1354–1374.

——, and R. T. Williams, 1987: Analytical and numerical studies of the beta-effect in tropical cyclone motion. Part I: Zero mean flow. *J. Atmos. Sci.*, **44,** 1257–1264.

DeMaria, M., 1985: Tropical cyclone motion in a nondivergent barotropic model. *Mon. Wea. Rev.*, **113,** 1199–1210.

Dong, K., and C. J. Neumann, 1986: The relationship between tropical cyclone motion and environmental geostrophic flows. *Mon. Wea. Rev.*, **114,** 115–122.

Emanuel, K. A., 1986: An air–sea interaction theory for tropical cyclones. Part I: Steady-state maintenance. *J. Atmos. Sci.*, **43,** 585–604.

Fiorino, M., and R. L. Elsberry, 1989: Some aspects of vortex structure related to cyclone motion. *J. Atmos. Sci.*, **46,** 975–990.

Frank, W. M., 1977: The structure and energetics of the tropical cyclone. Part I: Storm structure. *Mon. Wea. Rev.*, **105,** 1119–1135.

——, 1984: A composite analysis of the core of a mature hurricane. *Mon. Wea. Rev.*, **112,** 2401–2420.

George, J. E., and W. M. Gray, 1976: Tropical cyclone motion and surrounding parameter relationships. *J. Appl. Meteor.*, **15,** 1252–1264.

Gray, W. M., and D. J. Shea, 1973: The hurricane's inner core region. Part II: Thermal stability and dynamic characteristics. *J. Atmos. Sci.*, **30,** 1565–1576.

Gunther, E. B., and R. L. Cross, 1985: Eastern North Pacific tropical cyclones of 1984. *Mon. Wea. Rev.*, **113,** 1393–1410.

Hawkins, H. F., and D. T. Rubsam, 1968: Hurricane Hilda, 1964. Part II: Structure and budgets of the hurricane on 1 October 1964. *Mon. Wea. Rev.*, **96,** 617–636.

——, and S. M. Imbembo, 1976: The structure of a small, intense hurricane—Inez 1966. *Mon. Wea. Rev.*, **104,** 418–442.

Holland, G. J., 1984: Tropical cyclone motion: A comparison of theory and observation. *J. Atmos. Sci.*, **41,** 68–75.

Jorgensen, D. P., 1984a: Mesoscale and convective-scale characteristics of mature hurricanes. Part I: General observations by research aircraft. *J. Atmos. Sci.*, **41,** 1268–1285.

——, 1984b: Mesoscale- and convective-scale characteristics of mature hurricanes. Part II: Inner core structure of Hurricane Allen (1980). *J. Atmos. Sci.*, **41,** 1287–1311.

——, P. H. Hildebrand, and C. L. Frusch, 1983: Feasibility test of

an airborne pulse-Doppler meteorological radar. *J. Climate Appl. Meteor.*, **22,** 744–757.

——, E. J. Zipser, and M. A. LeMone, 1985: Vertical motions in intense hurricanes. *J. Atmos. Sci.*, **42,** 839–856.

La Seur, N. E., and H. F. Hawkins, 1963: An analysis of Hurricane Cleo (1958) based on data from research reconnaissance aircraft. *Mon. Wea. Rev.*, **91,** 694–709.

Leise, J. A., 1981: A multi-dimensional scale-telescoped filter and data extension package. NOAA Tech. Memo. ERL WPL-82, 20 pp.

Marks, F. D., Jr., and R. A. Houze, Jr., 1984: Airborne Doppler radar observations in Hurricane Debby. *Bull. Amer. Meteor. Soc.*, **65,** 569–582.

——, and ——, 1987: Inner core structure of Hurricane Alicia from airborne Doppler radar observations. *J. Atmos. Sci.*, **44,** 1296–1317.

Neldar, J. A., and R. Mead, 1965: A simplex method for function minimization. *Comp. J.*, **7,** 308–313.

Neumann, C. J., 1979: On the use of deep-layer-mean geopotential height fields in statistical prediction of tropical cyclone motion. *Proc. Sixth Conf. on Probability and Statistics in Atmospheric Sciences,* Banff, Amer. Meteor. Soc., 32–38.

Ooyama, K. V., 1987: Scale-controlled objective analysis. *Mon. Wea. Rev.*, **115,** 2479–2506.

Peng, M. S., and R. T. Williams, 1990: Dynamics of vortex asymmetries and their influence on vortex motion on a β-plane. *J. Atmos. Sci.*, **47,** 1987–2003.

Pike, A. C., 1985: Geopotential heights and thicknesses as predictors of Atlantic tropical cyclone motion and intensity. *Mon. Wea. Rev.*, **113,** 931–939.

——, 1987: A comparison of wind components and geopotential heights as statistical predictors of tropical cyclone motion. *Proc. 17th Conf. on Hurricanes and Tropical Meteorology,* Miami, Amer. Meteor. Soc., 101–103.

Powell, M. D., 1982: The transition of the Hurricane Frederic boundary-layer wind fields from the open Gulf of Mexico to landfall. *Mon. Wea. Rev.*, **110,** 1912–1932.

Rotunno, R., and K. A. Emanuel, 1987: An air–sea interaction theory for tropical cyclones. Part II: Evolutionary study using a nonhydrostatic-axisymmetric numerical model. *J. Atmos. Sci.*, **44,** 542–561.

Shapiro, L. J., 1983: The asymmetric boundary-layer flow under a translating hurricane. *J. Atmos. Sci.*, **40,** 1984–1998.

Shea, D. J., and W. M. Gray, 1973: The hurricanes's inner core region. I: Symmetric and asymmetric structure. *J. Atmos. Sci.*, **30,** 1544–1564.

Willoughby, H. E., 1988: Linear motion of a shallow-water barotropic vortex. *J. Atmos. Sci.*, **45,** 1906–1928.

——, and M. B. Chelmow, 1982: Objective determination of hurricane tracks from aircraft observations. *Mon. Wea. Rev.*, **110,** 1298–1305.

——, J. A. Clos, and M. G. Shoreibah, 1982: Concentric eye walls, secondary wind maxima, and the evolution of the hurricane vortex. *J. Atmos. Sci.*, **39,** 395–411.

——, F. D. Marks, Jr., and R. J. Feinberg, 1984a: Stationary and propagating convective bands in asymmetric hurricanes. *J. Atmos. Sci.*, **41,** 3189–3211.

——, H-L. Jin, S. J. Lord, and J. M. Piotrowicz, 1984b: Hurricane structure and evolution simulated by an axisymmetric, nonhydrostatic numerical model. *J. Atmos. Sci.*, **41,** 1169–1186.